Final Report

Project Title: "High Efficiency Nanostructured III-V Photovoltaics for Solar Concentrator Application"

Covering Period: Full Project (June 1, 2008 – April 30, 2012)

Date of Report: September 12, 2012

Recipient: Rochester Institute of Technology

Award Number: DE-FG36-08GO18012

Working Partners: University of California – Riverside

Computational Fluid Dynamics RC, Inc.

Cost-Sharing Partners:

Contacts:

Dr. Seth M. Hubbard - PI
Assistant Professor of Physics
(585) 475 – 4214
email: smhsps@rit.edu

Katherine A. Clark – Authorized Agent
Associate Director for Grants Management
(585) 475 - 7984
kacsrs@rit.edu

DOE Project Team:

DOE Field Contracting Officer - Andrea Lucero
DOE Field Project Officer - Bradley Ring
Project Engineer - Patricia Saito

Table of Contents

Project Objective:

The High Efficiency Nanostructured III-V Photovoltaics for Solar Concentrators project seeks to provide new photovoltaic cells for Concentrator Photovoltaics (CPV) Systems with higher cell efficiency, more favorable temperature coefficients and less sensitivity to changes in spectral distribution. The main objective of this project is to provide high efficiency III-V solar cells that will reduce the overall cost per Watt for power generation using CPV systems.

Executive Summary:

This project addresses the need for future high-efficiency PV cells for solar concentrator systems. The limits of what can be achieved using conventional device design and crystalline technology have been reached (essentially at the theoretical limits for single junction Si and GaAs PV cells). The current state-of-the art (SOA) CPV cells (multi-junction III-V devices) have a high degree of spectral sensitivity due to current matching requirements and severe materials constraints imposed by their epitaxial fabrication process. The next generation of III-V cells will incorporate nanostructured materials, which will increase the efficiency of solar conversion through quantum mechanical confinement effects. Nanostructures can be used to "tune" the semiconductor bandgap, electrical conductivity, density of states and even thermal conductivity. For example the optical bandgap of the device can be better optimized to the solar spectrum, allowing a greater portion of the available light to be harvested and resulting in increased efficiency and reduced thermal rejection.

Our technical approach leverages many years of NPRL research in solar power, nanomaterials development and III-V multi-junction cell growth. The Nanostructured III-V PV project capitalizes on a diverse team of senior researchers with experience in multi-junction III-V cell growth, nanomaterials synthesis, and photovoltaic device modeling and development. The program addresses future generation CPV requirements through the use of nanostructured materials. These types of cells will have a number of physical advantages over current technology (i.e. increased efficiency, simple design, reduced spectral sensitivity) and should result in a reduction in cost per watt for concentrator systems.

This work is focused both on a potential near term application, namely the use of indium arsenide (InAs) QDs to spectrally "tune" the middle (GaAs) cell of a SOA triple junction device to a more favorable effective bandgap, as well as the long term goal of demonstrating intermediate band solar cell effects. The QDs are confined within a high electric field i-region of a standard GaAs solar cell. The extended absorption spectrum (and thus enhanced short circuit current) of the QD solar cell results from the increase in the sub GaAs bandgap spectral response that is achievable as quantum dot layers are introduced into the i-region. We have previously grown InAs quantum dots by OMVPE technique and optimized the QD growth conditions. Arrays of up to 40 layers of strain balanced quantum dots have been experimentally demonstrated with good material quality, low residual stain and high PL intensity. Quantum dot enhanced solar cells were grown and tested under simulated one sun AM1.5 conditions. Concentrator solar cells have been grown and fabricated with 5-40 layers of QDs. Testing of these

devices show the QD cells have improved efficiency under concentration compared to baseline devices without QDs. Device modeling and measurement of thermal properties was performed by UC Riverside. Improvements in a triple junction solar cell with the insertion of QDs into the middle current limiting junction was estimated to be as high as 36% under one sun illumination for a 100 layer stack QD enhanced cell.

Significant Accomplishments during Phase 1 (pre-Go/No-Go) of this project:

1. QD enhanced solar cells were grown using 5-20-stacks of InAs QD inserted within the i-region of a GaAs p-i-n solar cell. Significant enhancement in one sun AM1.5d Jsc was observed in the QD enhanced cells. Under concentrated sunlight, the reduced (longer wavelength) effective bandgap of the QD enhanced solar cell should lead to direct improvement in cell efficiency. Results under concentration confirm the tuning ability of the QDs, with QD cell efficiency exceeding the baseline by 1% absolute at 400 sun concentration.
2. Improvements in a triple junction solar cell with the insertion of QDs into the middle current limiting junction was estimated using detailed balance theory and an experimentally measured 0.017 mA per QD layer increase in the J_{SC} of a GaAs solar cell. A one sun efficiency of 34.0% is predicted for a 40X QD enhanced TJSC. Increasing the number of QD layers beyond 40X gave 35.7% for a 100X QD enhanced TJSC and 38.7% for a 200X QD cell.
3. A modified continuum elasticity theorem (CET) was developed to model strain balancing in QD superlattice (SL). The modeled strain values and balancing condition precisely correlated with XRD measured values for QD-SL samples. This new model was used to predict the exact GaP strain compensation thickness for minimum stress.
4. A economical gold electroplating process was developed to increase gold grid finger thickness at reduced cost. The Au electroplating process was successfully incorporated into a typical concentrator solar cell fabrication process and produced excellent results. Peak efficiencies were obtained at greater than 400 suns as per design criteria as well as a corresponding drop in series resistance of the device. The economical impact of this procedure over typical metal evaporation was clearly demonstrated.
5. Models and measurements of temperature effects in QD solar cells show that the QD based solar cells are slightly less sensitive to variation in temperature.
6. A new module for NanoTCAD, a physics-based model at CFDRC, was developed to incorporate solar illumination on a standard GaAs solar cell. The model and RIT experimental data show excellent agreement.
7. University California Riverside: The temperature and dot-size dependence of the thermal conductivity of quantum dot structures (used for solar cells) was explained with the help of the phonon – hopping model. The heat in solar cell structures is mostly carried by acoustic phonons. Their transport is substantially different in quantum dot super-lattice structures from that in bulk semiconductors. The model is currently used for the thermal optimization of the nanostructured solar cells.

Summary of each Task during Phase 1 (pre Go/No-Go):

I. **Task 1:** Use metal organic vapor phase epitaxy to grow an array of strain-balanced InAs QDs. Optical characterization (PL), metrology (AFM) and x-ray diffraction (XRD) will be performed as necessary to optimize dot size, dot density and strain. The optimization will draw on previous QD growth results and will yield a uniform array of strain-balanced QDs. The number of stacked QDs will be maximized based on XRD measurements of strain.

The QDs used in this study were InAs grown using the Stranski-Krastanov technique. This method relies on the 7.8% compressive strain between InAs and the GaAs substrate. Due to the low interface energy of InAs on GaAs, layers start with an initial 2D-type growth. However, as the layer becomes thicker and strain increases, energy is minimized by formation of coherent (defect-free) 3D islands (QDs). The InAs QDs grown in this study had nominal dimension of 6 nm in height and 30 nm at the base. The atomic force microscopy (AFM) measured QD density was ~5×10^{10} cm^{-2}. Fig. 1 shows an AFM micrograph of uncapped QDs grown by the MOVPE process. The QDs typically align along the growth step edges when using vicinal substrates, as seen in Fig. 1. Reactor growth conditions such as temperature, flow and V/III ratio were optimized and have been reported [1, 2].

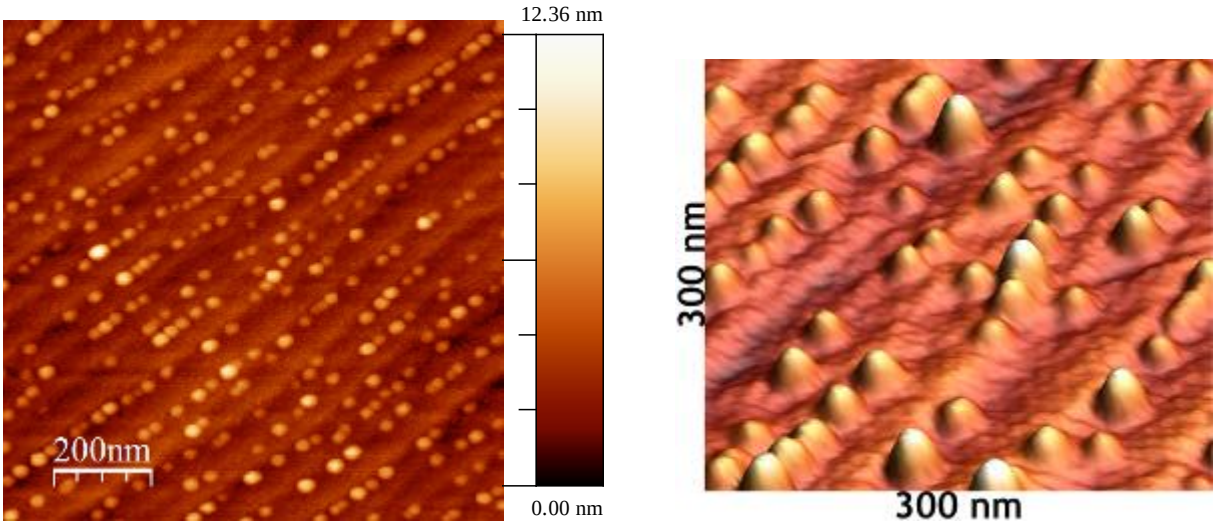

Fig. 1. Atomic force micrograph of the MOVPE grown InAs QDs used in this work. QD density was ~5×10^{10} cm^{-2} and average QD size was 6×30 nm.

The residual strain between each successive dot layer results in vertical ordering of the quantum dots, and is an essential element for increasing the absorption cross section of QD solar cells. However, the strain necessary to form SK based QDs can also lead to defect formation for stacked superlattice structures. In order to mitigate this, QD arrays

used in this study consist of a strain balanced superlattice structure. In direct analogy to quantum wells, the compensation of compressive strain intrinsic to SK QD systems can be realized by introducing a layer of tensile strained material. Due to the high lattice mismatch of the InAs/GaAs system, GaP was chosen for this layer, as its aggressive tensile mismatch (3.9%) allows for a 1-2 nm balancing layer, thus facilitating electronic transport through tunneling.

The strain balanced QD layer sequence is as follows. A layer of InAs QDs is grown and followed by a thin GaAs capping layer, a GaP strain compensation layer, and another thin layer of GaAs. In order to verify proper strain balance conditions, both high resolution X-ray diffraction (XRD) spectra and transmission electron micrographs (TEM) were taken of the samples. The XRD spectra were taken as $\omega/2\theta$ rocking curves around the (004) Bragg reflection. The TEM was taken in cross section parallel to the growth direction.

As seen in Fig. 2, the XRD spectra of a 10X stack of optimally strain balanced QDs shows clearly defined and intense satellite peaks indicating good material quality and superlattice periodicity. The zero order peak of the superlattice is nearly coincident with the GaAs substrate reflection. This is an indication of the strain-balanced condition in the QD superlattice. The inset in Fig. 2 shows the cross sectional TEM image. The InAs QDs are clearly visible and maintain roughly the same dimensions throughout the stack. The GaP layer is also visible and appears continuous. No threading dislocations were observed in the 10X stacks of QDs imaged by TEM.

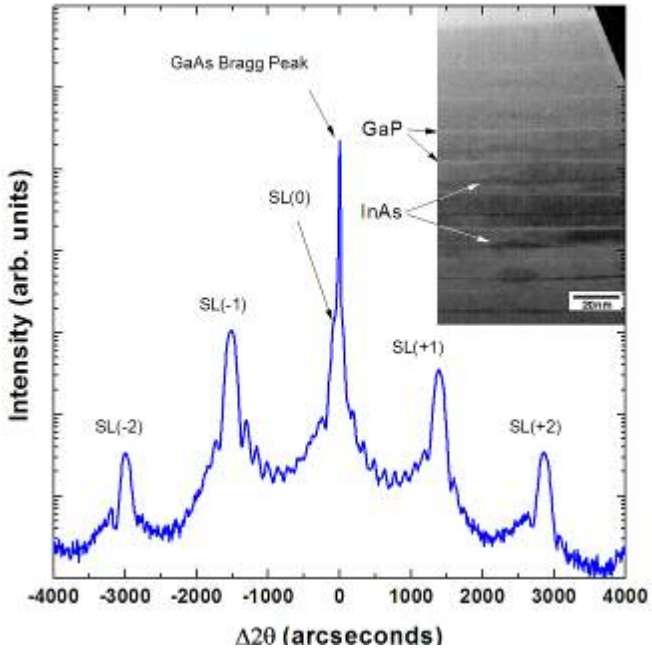

Fig. 2. X-ray diffraction ($\omega/2\theta$) spectra taken around the (004) reflection of GaAs. The inset shows a cross-sectional TEM image of the 10X stack of strain balanced InAs QDs.

In addition, we have developed a three dimensionally modified version of continuum elastic theory (CET) for the prediction of GaP thickness intended for the compensation of the strain induced by multiple stacks of SK-grown InAs QD on GaAs [3]. HRXRD was used to experimentally verify the appropriate strain balancing predicted by the modified theory. As seen in Fig. 3, a comparison of the measured in-plane strain and that predicted by both QW (standard CET) and our modified CET are shown. The 3D-modified CET theory gave the zero in-plane strain value at 4.2 ML of GaP. This model correlates well with the HRXRD data, in that a linear fit to this experimental data predicts approximately 4.5 ML.

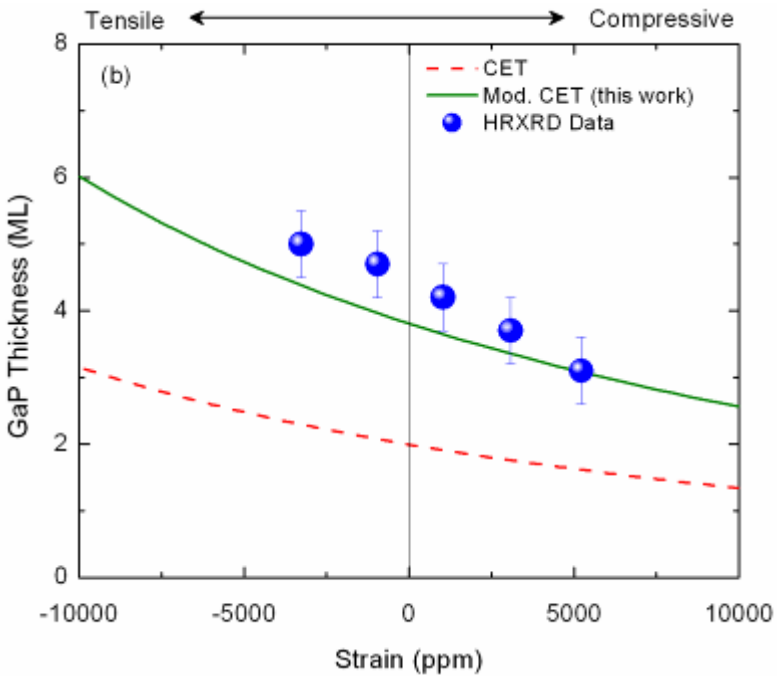

Fig. 3 Plot of GaP thickness in ML versus in-plane strain value of HRXRD data with CET QW theory and 3D-modified QD strain balancing theory.

II. **Task 2.** Growth of baseline and strain-balanced QD enhanced single junction GaAs pin solar cells. QDs will initially be embedded in the i-region of the cell. Cells will be characterized under one-sun Air Mass 1.5 conditions. Efficiency and related metrics will be measured. Characterization of the cells under concentration will be performed in order to gauge how QD cells efficiency, short circuit current and open circuit voltage are affected by high concentration conditions. Cell optimization will be performed as needed to improve cell performance under concentration.

Concentrator Cell Design and Economical Electroplating

We have developed a Au electroplating process to increase the gold grid finger thickness, thus reducing the device series resistance. Electroplating is a low complexity

and economical way to achieve thick gold layers, and can be easily integrated into a typical solar cell fabrication process. In contrast with evaporation which requires 1.75 grams for 1μm of gold (over a 1.04 cm2 area), electroplating 1μm of gold over the same area requires only 0.05 grams.

a) 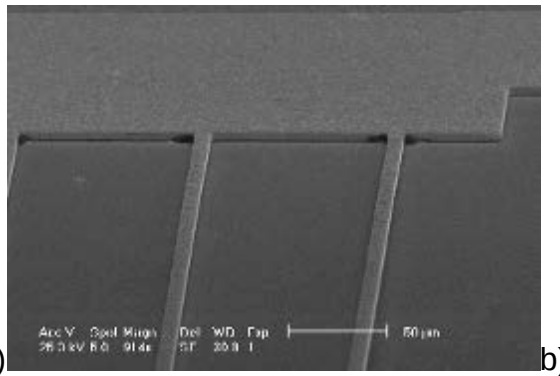

b) 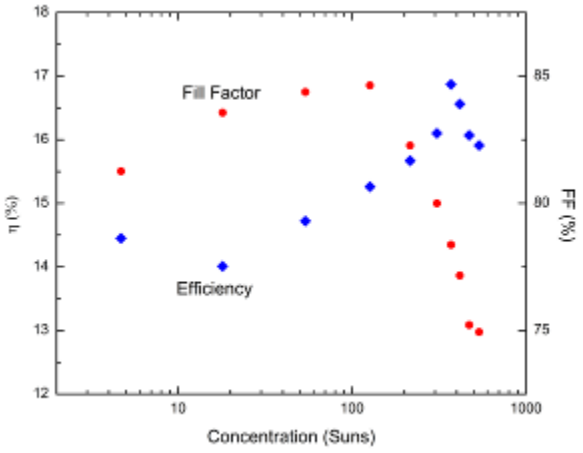

Fig. 4 a) SEM images show good morphology of plated fingers. b) Peak efficiency of 16.9 % at nearly 400 suns is close to the desired concentration for our cell design. This value remains constant within 1 % (absolute) out to over 500 suns.

Incorporating the Au electroplating process steps into our current fabrication process was successfully implemented, resulting in cells with a target 6 μm grid finger heights [4]. The morphology of plated gold, as evident from Fig. 4a, is similar to that of evaporated gold, with higher RMS surface roughness of near 1300 Å. This RMS height variation is insignificant compared with the height of plated fingers. The photoresist mold used eliminates lateral plating so finger widths can be sharply defined through prior lithographic steps.

At one sun, FF and efficiency differences between a 2 μm evaporated and 6 μm plated cells were not noticeable enough to be attributed to increased grid finger thickness. However, thicker fingers improve performance at higher concentrations, shown in Fig. 4b, with peak fill factor and efficiencies occurring near the design specified 400 suns.

To quantify the actual decrease in series resistance, the specific contact resistance and overall series resistance were obtained. Specific contact resistances (~4×10^{-5} Ω-cm^2) are comparable and overall sheet resistance (500 Ω/sq) is within acceptable tolerance. However, the overall series resistance has been reduced by over half that of the standard evaporated process (from 37 mΩ-cm^2 to 15 mΩ-cm^2) showing that for our cell design, resistance through the grid layer was dominant. These cells are now in the target range of overall series resistance to operate at near 400 to 500 suns as expected from PC1D simulations.

In addition to the Au plating study, we have also investigated improving the solar cell layer design for operation under high concentration. Increasing the emitter doping should reduce lateral distributed series resistance between grid fingers, thus increasing

fill factor and decreasing power loss at high concentration. Increasing the base thickness should increase current collection at high concentration. Both designs have been grown, fabricated and successfully tested under concentration conditions.

Using a model for quantum efficiency based on Hovel *et al.* [5] the spectral response of our GaAs concentrator solar cells was modeled, with lifetime, mobility, layer thicknesses, and doping levels as inputs. Fig. 5a shows a typical spectral response curve for parameters similar to our fabricated devices. The generated photocurrent under a given spectrum can be calculated, and along with expressions for the dark currents a J-V plot of the cell with given parameters is obtained. Combining this with grid optimization considerations allows power loss due to shadowing and series resistance to be incorporated into the model. The goal is to optimize together the layer structure, doping, grid structure and cell size to maximize efficiency at a desired concentration level. Fig. 5b is a preliminary plot of efficiency vs. cell area for a concentration of 400 suns. At each given area the same cell structure was used, whereas to be more accurate, at each area cell parameters should be optimized to achieve maximum efficiency for the device dimensions considered. The next step in this modeling is to incorporate the generation and recombination of quantum dots in the intrinsic region of the structure. This can be done simply by treating them as Gaussian like absorbers, but with more detailed consideration of their absorption properties. The goal is to identify the optimum number of quantum dot layers taking into account the increased generation of photocurrent and open-circuit voltage degradation.

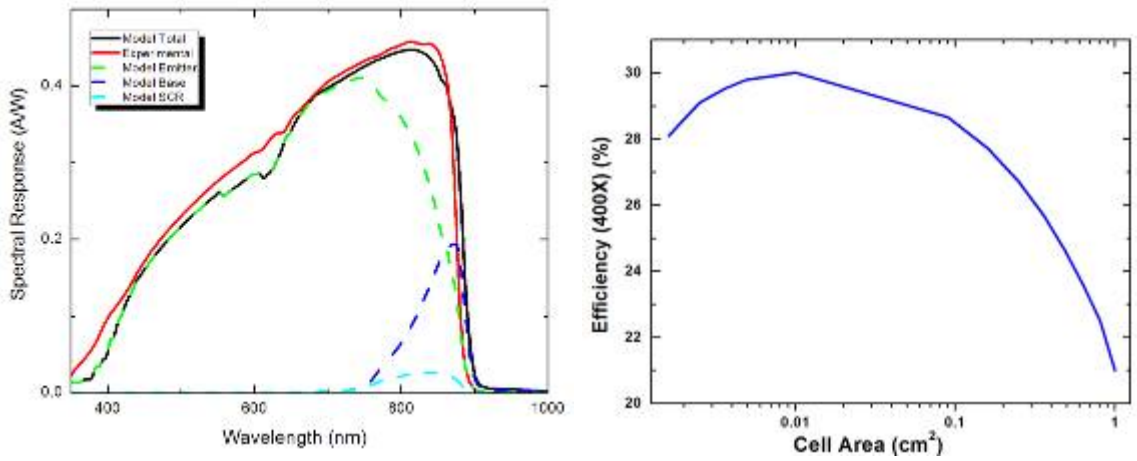

Fig. 5 a) modeled spectral response of GaAs cell showing contributions from all layers, and total spectral response, b) modeled efficiency vs device area at 400 suns

In addition, the modeling efforts are being applied to our work on electroplating the grid contacts. A commercial plating solution has been incorporated into our standard cell processing procedure. For operation of GaAs concentrators near 500 suns the grid layer thickness should be about 6 μm. For smaller device areas, high aspect ratio is necessary as grid finger width scales with device size. Using a high aspect ratio photoresist mold this can be achieved. Current concentrator grid design with 6-10 μm finger width and height will be scaled and optimized using the above modeling, and various size devices will be fabricated to maximize aspect ratio using the electroplating process.

Quantum Dot Enhanced Concentrator Solar Cells

In order to test the effectiveness of QD tuning of the middle junction material, a series of single junction (SJ) GaAs *p-i-n* solar cells were grown. The substrate used was a 350 μm thick vicinal *[100]* GaAs offcut at 2° towards the *[110]*. The QD and epilayer growth were performed on a Veeco P125LDM multi-wafer rotating disk reactor. Single junction *p-i-n* GaAs control (baseline) cells were grown without QD layers and with a GaAs i-region thickness of 100 nm. QD cells were grown with arrays of 5, 10 and 20 of QDs in the GaAs i-region using strain compensation values optimized in Task1. A new 0.5 cm^2 grid design was implemented based on the modeling results. Standard III-V processing techniques were used for device fabrication. Grid finger were electroplated gold as described above. AM1.5g and AM1.5d calibration standards were obtained from the National Renewable Energy Lab (NREL) prior to testing these devices.

Fig. 6 shows the illuminated one sun AM1.5g current density-voltage (JV) curves for a baseline GaAs cell without dots and for 5X, 10X and 20X layer strain balanced QD solar cells. The baseline cell gave results at or near our standard values for GaAs solar cells (see Table 1 results). An enhancement in short circuit current density (J_{SC}) using QDs is clearly visible. In fact, all QD cells show an improvement in J_{SC} compared to the baseline, with a clear increasing trend in J_{sc} versus number of QD layers. The increased Jsc of the device is a direct result of photo-generated current contributed by the QDs [1]. The trend with addition of QD is expected as a greater portion of the sub-GaAs bandgap solar spectrum should be absorbed with increased number (i.e. volume) of QDs. Additionally, the strain balancing technique employed for QD growth has resulted in higher material quality in layers grown on top of the QDs. This has made possible the short circuit current enhancement and minimal open circuit voltage degradation [1].

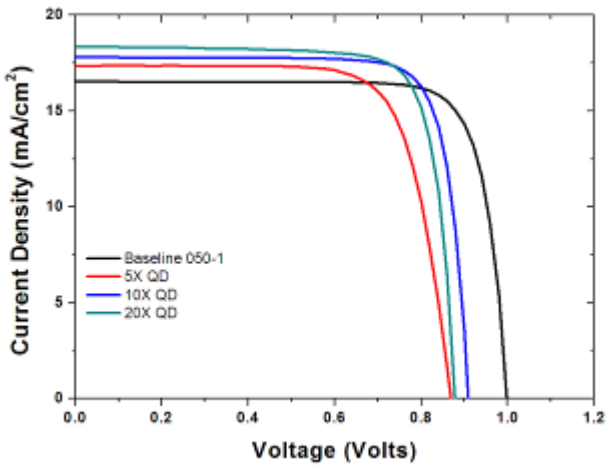

Table 1. One Sun AM1.5g Parameters

	I_{sc} (mA/cm^2)	V_{oc} (Volts)	FF (%)	Efficiency (%)
Baseline	**16.5**	**1.00**	**81**	**13.4**
5X	**17.3**	**0.87**	**74**	**11.2**
10X	**17.8**	**0.91**	**81**	**13.1**
20X	**18.3**	**0.89**	**80**	**12.8**

Fig. 6. One sun AM1.5g light J-V curves for the baseline GaAs *p-i-n* cell and 5X-20X QD cells.

The solar cells response was spectrally resolved in order to further investigate the current enhancement and the potential contribution from QDs. Shown in Fig. 7 is the external quantum efficiency (EQE) for the baseline and 5-20X QD samples. All three QD samples show an increase in response at wavelengths greater than the GaAs bandedge. This indicates that a portion of the three QD cell's short circuit current is being generated by QD related absorption processes. Additionally, as the number of QD layers is increased, the EQE at all QD related transitions is increased. As can be seen in Fig. 7, at 909 nm (1.36 eV) this amounted to increases from 2.5 to 9.2% by increasing the QD staking from 5X to 20X. This was clear evidence that increasing the volume of QDs absorbers is resulting in successively increasing short circuit current.

Electroluminescence was also collected for all samples. Shown in Fig. 7 is the spectrum for the 20X QD cell under an 1.6 A/cm^2 drive current (similar spectra were obtained for the 5X and 10X). Multiple QD related peaks were extracted from this curve at 1.18, 1.24, 1.29, 1.33 and 1.36 eV. These are consistent with numerous reports on InAs QD related optical transitions [6].

Similar peaks are observed in the EQE at most of the EL extracted transitions. However the EQE was observed to decline in intensity with increasing wavelength while EL data shows the opposite trend. This is representative of the fact that EQE represents both absorption of photons and collection of the carriers while EL represents only radiative recombination. Collection of carriers in QD cells occurs through both phonon and photon interaction with the QDs, thus deeply confined levels, such as the 1.18 eV transition, lack either sufficient phonons or photons to provide carrier extraction. However, measurement of EQE under an intense broadband light bias could perhaps improve the QD response in this range.

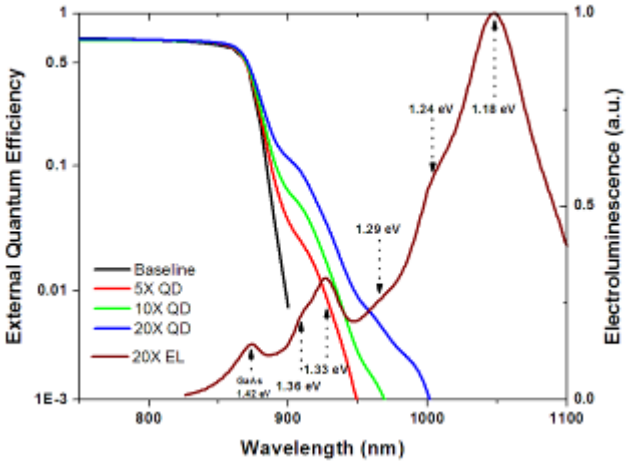

Fig. 7. Spectral Response and Electro-luminescence

In order to test the spectral tuning ability of the QDs at higher concentration, results were obtained under high intensity illumination using the LAPSS system at NASA Glenn Research Center. As seen in Fig. 8, the trends in short circuit current observed at one sun continue at high concentration, with QD cells showing enhanced short circuit currents. All cells, including the baseline, show a slight superlinear trend in current, as

has been observed in GaAs materials due to high level injection effects [7]. The 20X QD cell gave the highest short circuit current, 7.53 A/cm^2, of all the cells at 440X. This represents an 11% increase in the short circuit current compared to the baseline current at the same concentration.

In addition, the open circuit voltage versus concentration was fit to the following relation derived from the diode equation:

$$V_{OC}(C) = V_{oc}(1) + n\frac{kT}{q}\ln(C) \qquad (2)$$

where n is the diode ideality factor. As seen in Fig. 8, all cells show a good fit to this relation with an extracted ideality near 1.4. This number is indicative of cells operating with Shockley Reid Hall (SRH) recombination in both the quasi-neutral region and depletion/intrinsic region. The fact that the ideality deviates slightly from 1 may indicate a slightly higher perimeter area recombination related to processing. However, all cells show similar ideality and should be equivalent for comparison purposes.

The efficiency and fill factor for each type of cell was calculated under AM1.5d conditions and is shown in Fig. 8. Fill factor was observed to peak near 100-200X while efficiency peaked near 400X for most cells. This was consistent with our grid design.

The QD enhanced cell gave near 18% power efficiency at 400X. This represented a ~1% absolute efficiency improvement compared to the baseline (6% relative improvement). Under concentrated sunlight, the reduced (longer wavelength) effective bandgap of the QD enhanced solar cell leads to direct improvement in cell efficiency. This directly correlated to our detailed balance trend seen in Fig. 1. The enhanced efficiency of the QD cells were a result of the enhanced J_{SC} combined with minimal V_{OC} loss.

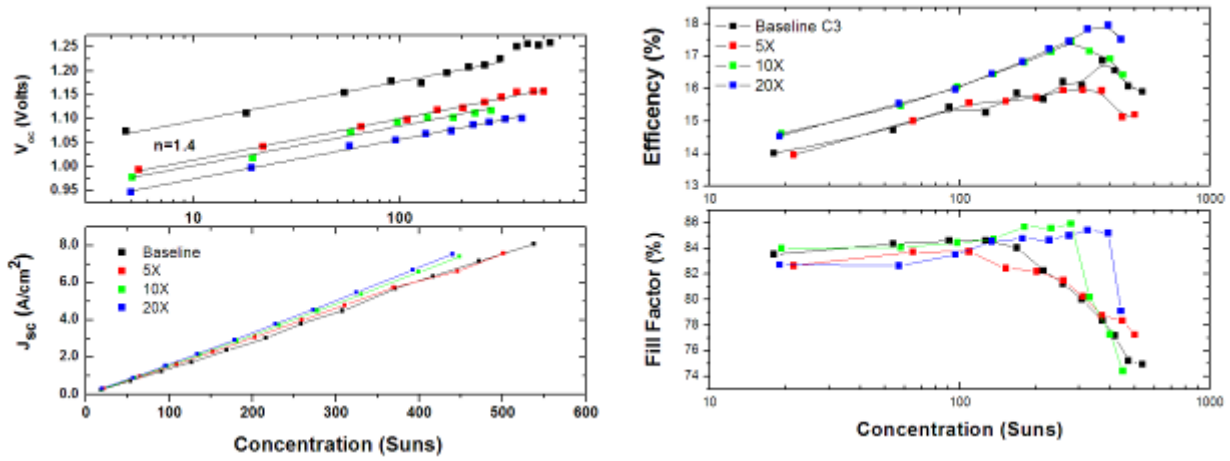

Fig. 8. a) AM1.5d open circuit voltage and short circuit current versus concentration for the baseline and QD cells. b) AM1.5d efficiency and fill factor versus concentration for the baseline and QD cells.

III. **Task 3.** Initial models for QD enhanced solar cells will be developed using the CFD Research Corporation modeling suite and compared to our above experimental results. In order to confirm model, standard GaAs pin solar cells (w/o QD) will also be modeled and compared to experimental results for our baseline cells.

Rochester Institute of Technology

The evaluation of the commercially available, physics-based, device simulation software Silvaco ATLAS for use in advanced photovoltaics analysis was performed. Results were used to optimize device parameters (doping and layer thickness). Experimental results and the ATLAS simulation of the optimized solar cell structure are shown below in Fig. 9. The application of this tool using our single-junction GaAs solar cell design and comparison to experimentally measured results indicates that i) the current design used in experimental work is optimized and ii) the ATLAS simulation program can accurately simulate solar cell device structures. We are currently working to extend the program to include concentration effects.

Table III

Device Metrics of the Optimized p-i-n Cell conditions

Ref. for InGaP n, k	V_{oc}	I_{sc}	P_m	FF	η
ATLAS Simulation	1.040 V	24.52 mA	21.40 mW	83.92 %	15.67 %
Experiment	1.043 V	24.71 mA	21.58 mW	83.73 %	15.80 %

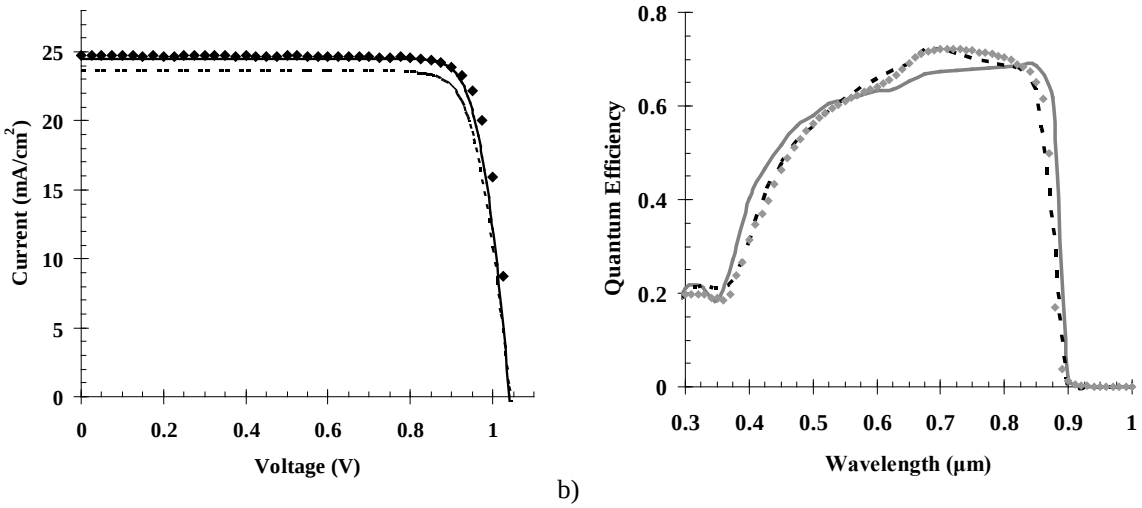

a) b)

Fig. 9. Electrical results of the optimized p-i-n solar cells compared to ATLAS simulations for a) illuminated current vs voltage and b) external quantum efficiency.

CFD Research Corporation

Further extension of modeling is being pursued using the physics-based NanoTCAD package at CFDRC. This simulator has the capability for both quantum mechanical and standard drift-diffusion physics-based modeling. As a first step, the modeling of a baseline (w/o QD) cell was conducted with 3D NanoTCAD device simulator, using the quantum level computed transport parameters for the i-layer (eventually QD will be added to this region in the model), while for other device regions, the classical drift-diffusion models were used. Comparison with the experimental data for baseline GaAs cells developed at RIT are shown in Fig. 10. As can be seen, the model gives a good fit. The lower part of the I-V curve is not ideally matched, possibly due to surface and interface recombination effects. However, some deviation at low currents was deemed acceptable in light of the fact concentrator solar cell normally operates at higher voltages and currents, close to the P_{max} (near V_{oc} and J_{sc}).

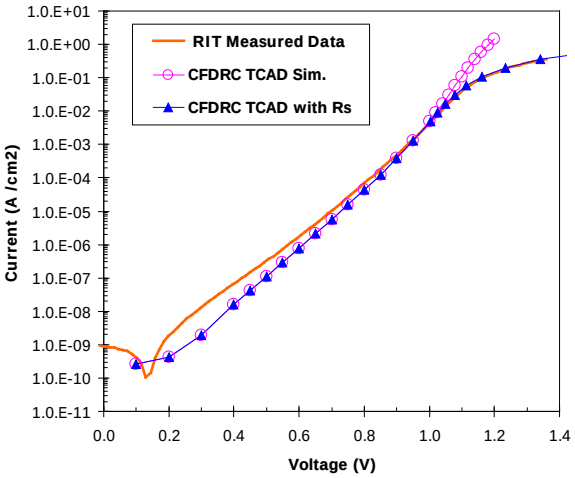

Fig. 10 CFDRC NanoTCAD model of a GaAs p-i-n solar cell dark J-V and comparison to RIT measured data.

CFDRC has implemented a new, advanced, physics-based photoabsorption model in NanoTCAD and is testing it compared to RIT GaAs solar cell data. The Fig. below (Fig. 11) shows the modeled spectral response and EQE and an RIT measured experimental EQE. The model shows a good fit to the baseline GaAs response but shows some improvements are still necessary in modeling optical response of the InGaP windows (dip in spectrum at 670 nm). RIT has provided CFDRC with measured optical response of InGaP and CFDRC is currently incorporating this into the NanoTCAD model.

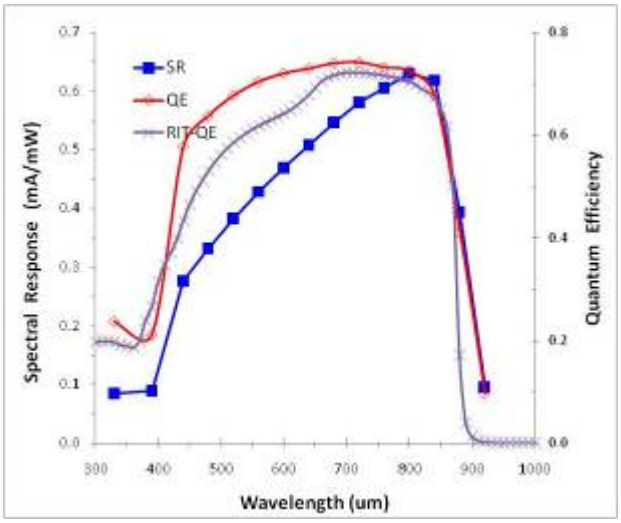

Fig. 11. CFDRC model of spectral response in comparison to RIT measured results.

University of California Riverside

The UCR team carried out physical modeling and computer simulation work to assist in the development of the quantum dot enhanced solar cells and the intermediate band solar cells. As it was shown in Balandin group's previous work, 3D ordered quantum dot superlattices (QDS) can be used for implementation of the intermediate band solar cells with significantly enhanced efficiency [8]. At the same time, the state-of-the-art OMVPE technology leads to QDS with relatively small quantum dot density in the grow plane and rather large inter-dot distance. These factors result in relatively small wave function overlap and weak coupling. The dot density is high enough only in the growth direction. For the present project it was important to simulate the performance of the QDS structure when the dot sizes and inter-dot distances are rather far from ideal. We assumed conical quantum dots with the dot base of 10 nm, dot height of 4 nm, and the inter-dot distance (along z direction) of 2 nm. The QDS parameters are realistic and close to those in the structures grown by RIT team. Under fully concentrated light: V_m=1.39V; J_m=2.6994×10^7(A/m^2); and the efficiency is ~ 51 %. Under one sun: V_m=0.95V; J_m=56.6mA/cm^2; and the efficiency is ~ 33%. This indicates that strong electron wave function overlap is essential for achieving a strong efficiency enhancement.

IV. **Task 4.** Measure the dark and light (AM1.5) current versus voltage behavior and the spectral response of GaAs-based pin solar cells with and without an InAs quantum dot array in the intrinsic region as functions of temperature. Temperature coefficients will be determined for QD enhanced GaAs pin solar cells. Thermal conductivity and behavior will be both experimentally and theoretically analyzed with the goal to predict and enhance operation of the QD cell under concentration and high temperature conditions.

In Fig. 12a, the temperature dependence of the spectral responsivity of a single junction GaAs cell with 40 layers of QD is shown. The bandedge of the GaAs junction follows uniformly with typical temperature dependent bandedge shifting for bulk materials. Correspondingly, the sub-GaAs bandgap quantum dot/wetting layer peaks redshift with increasing temperature with slightly lower temperature sensitivity. This shifted QD temperature dependence is indicative of conduction and valence band offset following a slightly different bandgap temperature-dependent expansion in comparison with the bulk host bandgap. This effect is primarily due to QD confinement, and can be seen in Fig. 12a, as the QD sub-gap peak becomes systematically enveloped by the bulk bandedge with increasing temperatures. Because of this effect, the resolution of the QD peaks becomes clearer at lower temperatures.

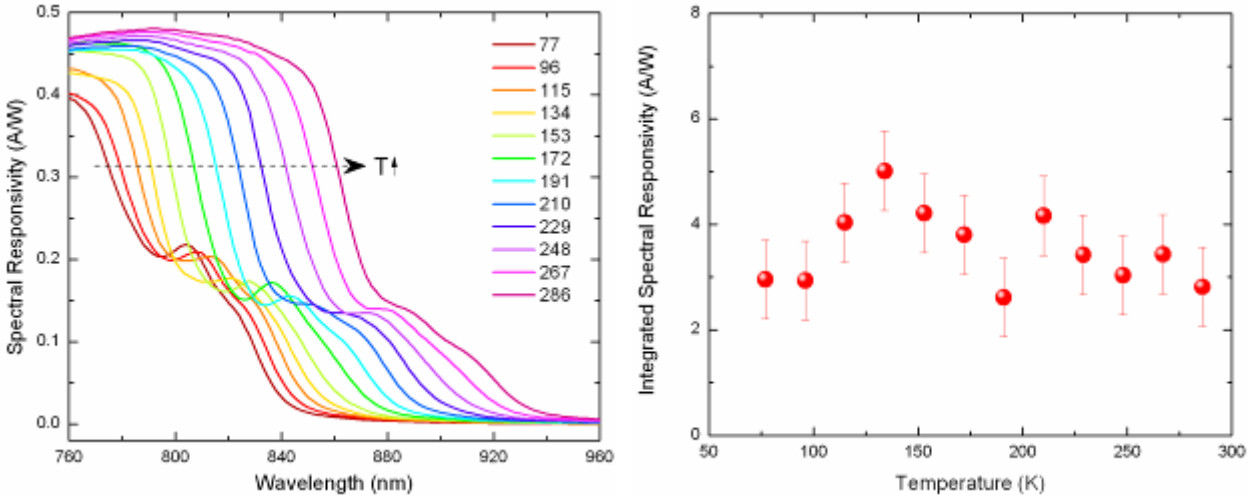

Fig. 12 a) Spectral Response as a function of temperature for a 20X QD enhanced solar cell. b) interated specral responsivity for QD related absorption as a funtion of temperature.

A fitting routine was used to deconvolve the spectral responsivity of the two apparent QD peaks and the bulk bandedge shown in Fig. 12a, for each temperature. As temperature increases, the peak responsivity energies of the InAs nanostructures decreases in a trend similar to the expected bandgap versus temperature relationship for GaAs. The temperature dependence of the absorption coefficient was determined from the spectral responsivity through the following relationship:

$$SR = q\int_0^\infty \frac{1}{E}\alpha(E)\left[1-R(E)\right]dE$$

Here, $\alpha(E)$ is the energy dependent absorption coefficient and $R(E)$ is the surface reflectivity of the device. Integrating under the Gaussian fits was performed to determine the relative absorption of the nanostructures as a function of temperature. Fig. 12b shows the integrated spectral responsivity values as a function of temperature. Here, it is apparent that there is no extractable trend with temperature, indicating any increase in absorption shown in Fig. 12a, is merely due to the proximity to the bulk

bandedge artificially enhancing the QD responsivity through convolution of bandtail states in the bulk. This is a relatively encouraging result, as enhancing the temperature insensitivity of solar cells may be beneficial to those operating under concentration.

The baseline and 5-20X QD cells from the previous concentration studies were measure under AM1.5D spectrum (1 sun JV) as a function of temperature. Temperatures varied from 278K-358K in 10K steps (5C-85C° in 10C° steps). Due to the GaAs bandgap dependence on temperature, we expect to see a linear increased in I_{SC} and decrease in V_{OC} with increasing temperature for the temperature range studied. The FF (and thus efficiency) also show linear dependence based on changes in resistivity with temperature.

Temperature coefficients were extracted for Isc, Voc, FF and efficiency. The results are shown below in Fig. 13 and Table 2. The short circuit current temperature dependence decreased slightly with incorporation of QDs. There was also a slight increase in open circuit voltage temperature dependence with QD incorporation. This behavior would be consistent with some portion of the spectrum being converted by the less temperature dependant QD array. The FF and efficiency compared between the baseline and 5X cell both show a decrease with temperature and roughly consistent results. Current efforts are underway to model the temperature coefficients of the baseline and QD cells using physics-based modeling.

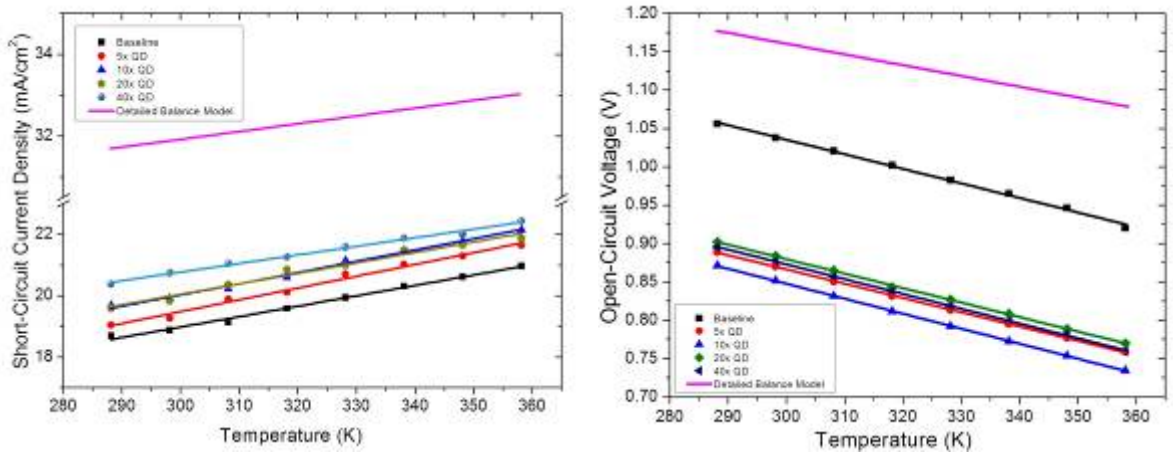

Fig. 13. I_{SC} and V_{OC} temperature dependence for the baseline, 5X QD and 20X QD concentrator cells (0.5 cm^2 active area, no AR coating).

Table 2: Temperature coefficients extracted for baseline, 5X and 20X QD concentrator cells.

Cell	Efficiency (%/K)	Fill Factor (%/K)	Jsc (µA/K)	Voc (mV/K)
Baseline	**-0.016**	**-0.05**	**30+/-1**	**-1.89**
5x QD	**-0.018**	**-0.08**	**38+/-2**	**-1.86**
10x QD	**-0.019**	**-0.06**	**36+/-1**	**-1.95**
20x QD	**-0.020**	**-0.07**	**34+/-2**	**-1.89**
40x QD	**-0.026**	**-0.07**	**28+/-1**	**-1.93**
Detailed Balance	**-0.035**	**-0.04**	**19**	**-1.4**

Temperature-dependent changes in the J-V curves of photodiodes contain information on QD-related related characteristics. The newly acquired Janis temperature controlled probe staion was used to collect light (~1 sun AM0) and dark J-V curves for a baseline *p-i-n* cell and a 5x QD device at temperatures between 80 and 400 K. The saturation current (J_0) and ideality factor (n) were extracted from fits of the n=2 region in each J-V curve. Arrhenius plots of J_0 against the inverse of temperature yield an activation energy, which is related to effective bandgap. The activation energy of the baseline cell is determined to be 0.80 eV. The QD-enhanced sample yields a lower value of 0.59 eV, which supports the band-gap narrowing with QD tuning. This change in activation energy suggests that carrier recombination takes place predominantly in the QD region of the sample—a conclusion corroborated by the relative intensity of electroluminescence at QD wavelengths.

University of California Riverside

The use of nanostructured solar cells for CPV systems raises the issue of efficient heat removal from photovoltaic cells. At the University of California Riverside, an experimental investigation of the thermal conductivity of a standard GaAs-based p-i-n solar cells without quantum dots and with 5X-layers of InAs QD and SB-QD was performed. The results obtained for the reference and quantum dot solar cell structures were compared with the thermal conductivity of bulk GaAs crystals (see Fig. 14). The thermal conductivity of the reference solar cells is larger than that of quantum dot solar cells by about a factor of 2. However, the thermal conductivity of the reference and quantum dot solar cells slowly increases with temperature T. This is in contrast to the ~1/T-type dependence of the thermal conductivity of bulk crystal semiconductors.

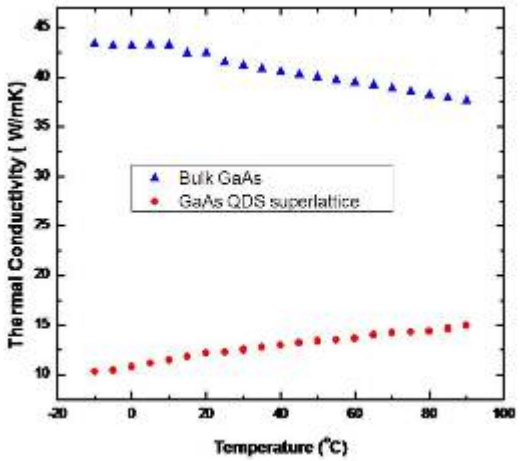

Fig. 14. Measured thermal conductivity of bulk GaAs and a GaAs QD superlattice.

V. **Task 5**: Use in-line atmospheric attenuation filters to measure performance and spectral response of cells as a function of changing atmospheric conditions. This

will be done using both a baseline SJ GaAs cell, a QD enhanced GaAs cell and a full commercially produced triple-junction baseline.

Our original solar simulator (Newport 450W solar simulator) had a good match to the AM0 and AM1.5 spectrums in the visible, but a poor match to both AM0 and AM1.5 spectrums in the infrared due to atomic transition lines in the Xe bulb spectrum. This resulted in less accurate results when measuring multi-junction cells. Task 5 required a new solar simulator with better spectral match to the AM1.5 spectrum. An 18 kW, two source solar simulator from TS Space Systems was acquired through separate Dept of Energy funding in collaboration with former co-PI Ryne Raffaelle (Raffaelle is currently not able to serve as co-PI as he recently became an employee of the DoE). This system has two light sources to improve spectral match to multi-junction cells as well as capability for both AM0 and AM1.5 spectrums. The beam size of the simulator is 300mm. A schematic showing the simulator is seen below in Fig. 15. The UV-VIS lamp is a metal halide and the IR lamp is a quartz tungsten halogen.

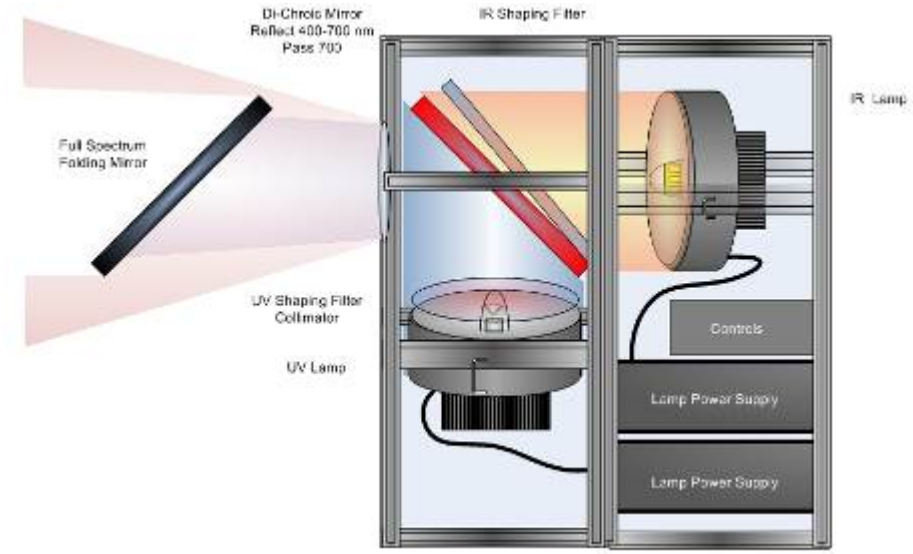

Fig. 15. Schematic of the TS Space System solar simulator.

Irradiance spectrums were taken using both the custom designed one sun AM0 and AM1.5 filters. As can be seen, a Class A close-match was measured in both cases. In addition, an Emcore Photovoltaics triple junction concentrator cells (CTJ) was measured using the improved spectral match conditions. The IV curve and extracted metrics under one sun are shown below and compared to nominal 1 sun values given by Emcore. As setup and calibration of this tool was necessary before completion of Task 5, we are currently in the process of measuring our GaAs and QD enhanced GaAs as a function of spectrum and atmospheric conditions.

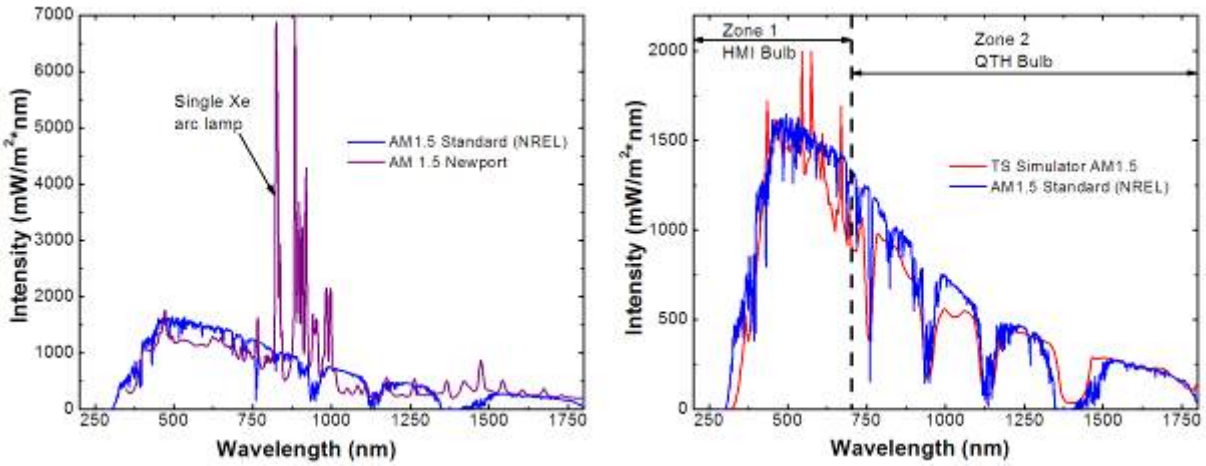

Fig. 16 a) AM1.5 irradiance using Newport Xe solar simulator, b) AM1.5 irradiance using TS Space system solar simulator. Both are compared to a standard AM1.5 irradiance spectrum obtained from NREL.

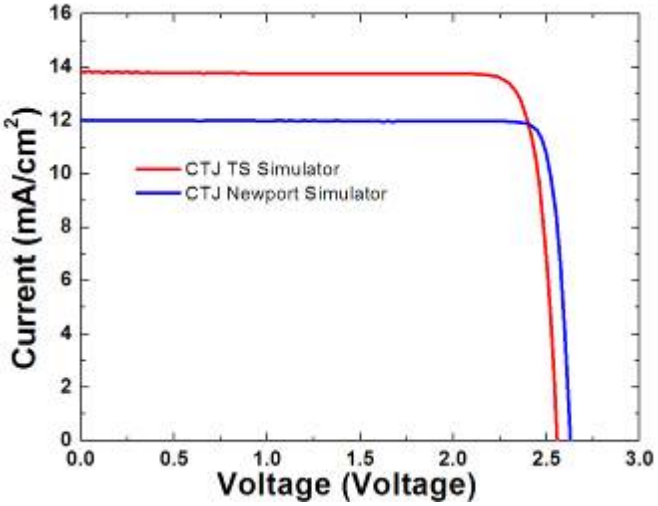

Fig. 17. Emcore CTJ receiver measured under one sun using the Newport and the TS Space System solar simulator.

Table 3. Comparison of results for the Emcore CTJ receiver.

	Emcore CTJ Nominal Values	**Newport Simulator measured values**	**TS Simulator measured values**
Efficiency (%)	31.4	28.6	30.8
Voc (V)	2.61	2.63	2.56
Jsc (mA/cm^2)	13.9	12.0	13.8
Vmax (V)	2.33	2.43	2.30
Jmax (mA/cm^2)	13.4	11.8	13.4
Maximum Power (mW)	31.4	28.6	30.8

VI. Task 6: Initial numerical models will be used in conjunction with previous results to develop QD enhanced pin solar cell numerical models. Based on these model results we will further optimize our device structure (QD size, density, stacking, layer thickness, etc.) for high concentration conditions.

The single junction limiting efficiency of a solar cell was calculated using detailed balance and the numerical AM1.5d spectrum. Shown below in Fig. 18a-c are calculations of maximum efficiency versus bandgap for various temperature and concentration levels under AM1.5d illumination. As CPV are intended for higher temperature application, we have simulated the efficiency from 250K (-23C°) to 400K (127C°). As can been seen, the maximum efficiency is near 35% at 250K but drops to 29% at 400K. This is a direct effect of the increased dark current at higher cell temperature. Additionally, a slight shift in optimal bandgap is observed with increasing temperature, again due to increased dark current.

At higher concentration, the reduction in peak efficiency is still present. For the temperature range 250-400K, peak efficiency degraded from 40% to 35% at 100 suns and from 42% to 37% at 1000 suns. However, at higher concentration, the illumination current plays a greater role than dark current, leading to relative insensitivity of the peak bandgap versus temperature. Thus, at 100-1000 suns, peak efficiency is still centered near 1.1 eV. Use of InAs QDs for bandgap tuning should still be effective at elevated temperatures. In fact, due to the 0D density of states inherent to QDs, we expect relatively little temperature sensitivity of the QD structures.

Detailed balance models were performed using both a 6000K blackbody as the illumination source and the ASTM numerical AM1.5g spectral data (obtained from NREL's website). We have simulated a standard triple junction solar cell using a Ge bottom cell and allowing the middle and cell bandgaps to vary. Seen in Fig. 19 are the iso-efficiency contours for both 6000K and AM1.5g spectrums. Also shown is a point indicating the current state of the art lattice matched InGaP/GaAs/Ge structure. The peak efficiency (47%) under the 6000K occurs at a middle cell bandgap of 1.21 eV and top cell bandgap of 1.85 eV. The peak efficiency (50%) under AM1.5g is much more broad, giving higher efficiency over a larger bandgap range. It also shows a shift in peak efficiency to 1.18 eV and 1.74 eV for the middle and top cell bandgaps, respectively. In both cases, the middle InGaAs junction is current limiting and therefore it is the efficiency limiting junction. As discussed in the original proposal, lowering the effective bandgap of the InGaAs middle cell in a lattice-matched triple junction can be achieved through the incorporation of an InAs QD array into the depletion region of an InGaAs cell However, in the AM1.5g, the InGaP top cell provides some limitation as well. Reduction of the top cell bandgap could also be accomplished using QD technology.

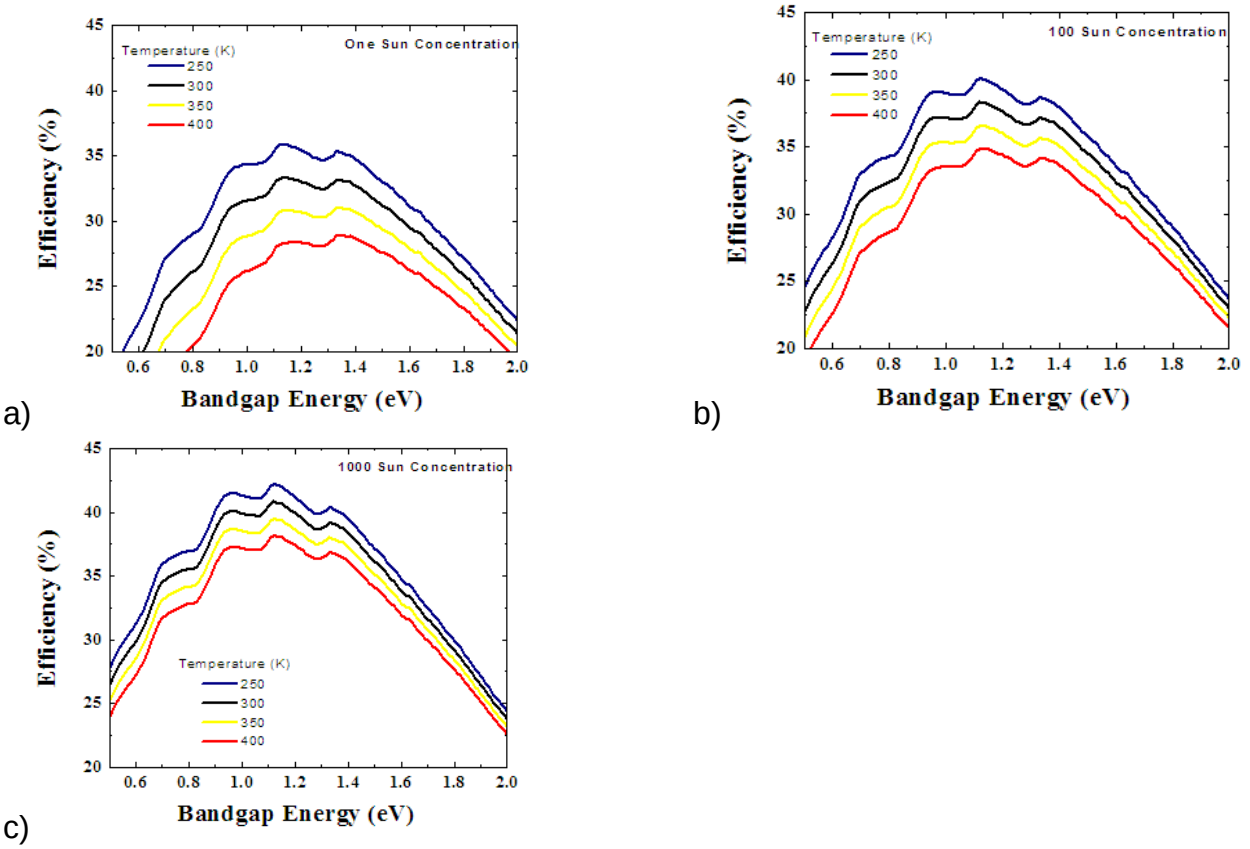

Fig. 18. Detailed Balance Model showing change in maximum efficiency with increasing temperature under a) 1Sun, b) 100 Sun and c) 1000 Sun concentration.

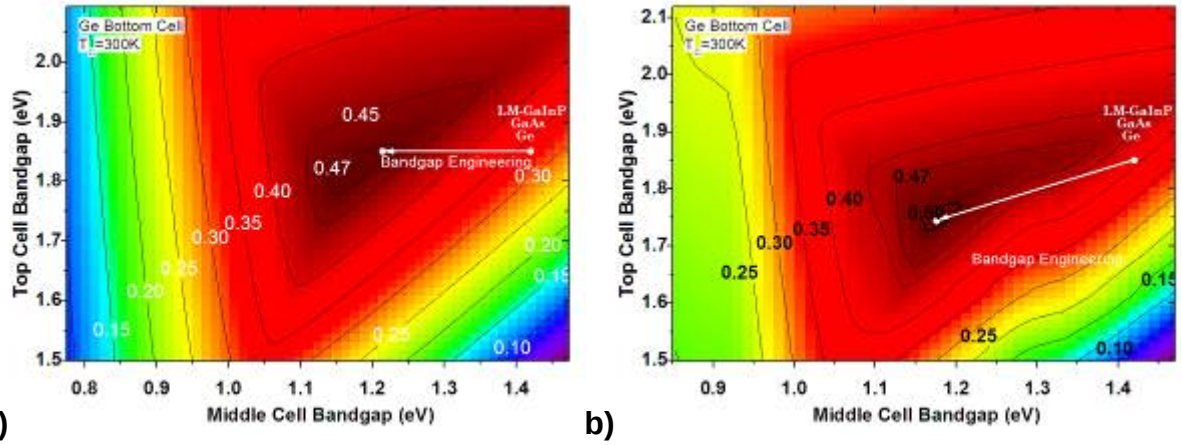

Fig. 19 Iso-efficiency contours for a triple junction solar cell under a) 6000K blackbody and b) true AM1.5g spectra

In addition, a full intermediate band solar cell was simulated using detailed balance and the AM1.5d spectrum. This simulation was conducted as a function of the intermediate band energy. The contour plots in Fig. 20 show the 1, 100 and 1000 sun

AM1.5d maximum efficiency of the IBSC design for various values of E_{CI} and E_{IV} (note that the host bandgap E_{CV}= E_{CI}+E_{IV}). Under the terrestrial AM1.5d spectrum, the water and CO_2 based absorption bands give rise to number of local maximum points in IBSC bandgap vs efficiency. This result shows that a wide range of QD materials could be useful for IBSC design, giving more flexibility to choice of materials.

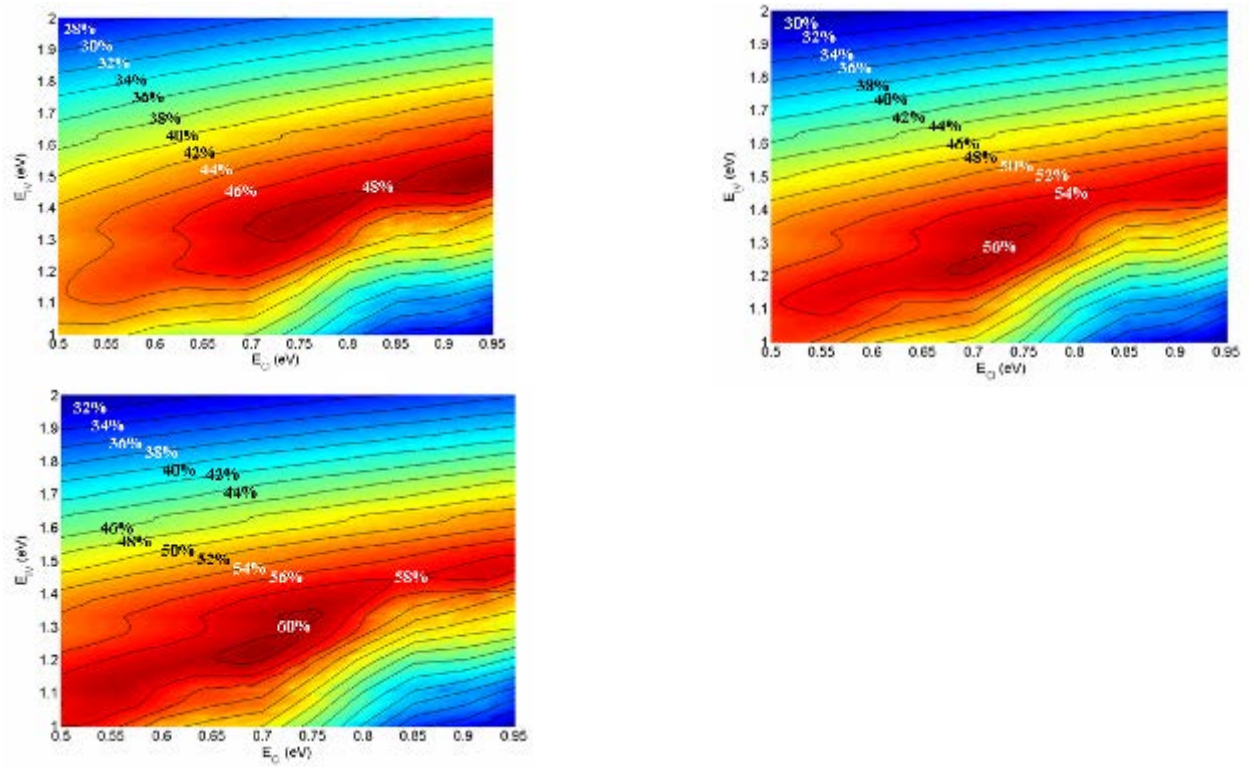

Fig. 20. Efficiency contours for the IBSC design using AM1.5d spectrum and concentration factors of a) 1 b) 100 and c) 1000 suns.

CRITICAL MILESTONE [GO/NO-GO DECISION]

- Budget Period 1 will close 18 months from the project start date. At this point, the Rochester Institute of Technology will have fabricated a quantum dot enhanced GaAs solar cell and measured this cell under Air Mass 1.5 conditions (one-sun and variable concentration). This cell will show enhanced short circuit current and minimal open circuit voltage degradation such that if this cell were used as the middle junction of standard InGaP/GaAs/Ge triple junction cell, the overall efficiency of the triple would be increased. The “current tuning” of the GaAs solar cell, using QDs, is the go/no-go decision criteria as this is the basic physical proof that QDs can be used to enhance the efficiency of a triple junction solar cell. Rochester Institute of Technology will deliver 5 QD enhanced GaAs

solar cells to the National Renewable Energy Laboratory (NREL) for independent testing and verification under Air Mass 1.5 conditions.

Using quantum efficiency (EQE) data from previously grown and fabricated QD SC with 5x-40x layers of InAs QDs (see Task 2 data above) and integrating the EQE convolved with the solar spectrum over the range of 880 nm-1000 nm yields the QD photocurrent enhancement (J_{SC-QD}) of the overall short circuit current (Fig. 21a). A slight residual current (0.1 mA/cm^2) is calculated for the baseline cell due to the thermal distribution of carries near the bandedge. However, a clear liner trend was calculated for J_{SC-QD} with increasing QD layers. This trend was fit using linear regression and a slope of 0.017 mA per QD layer was extracted.

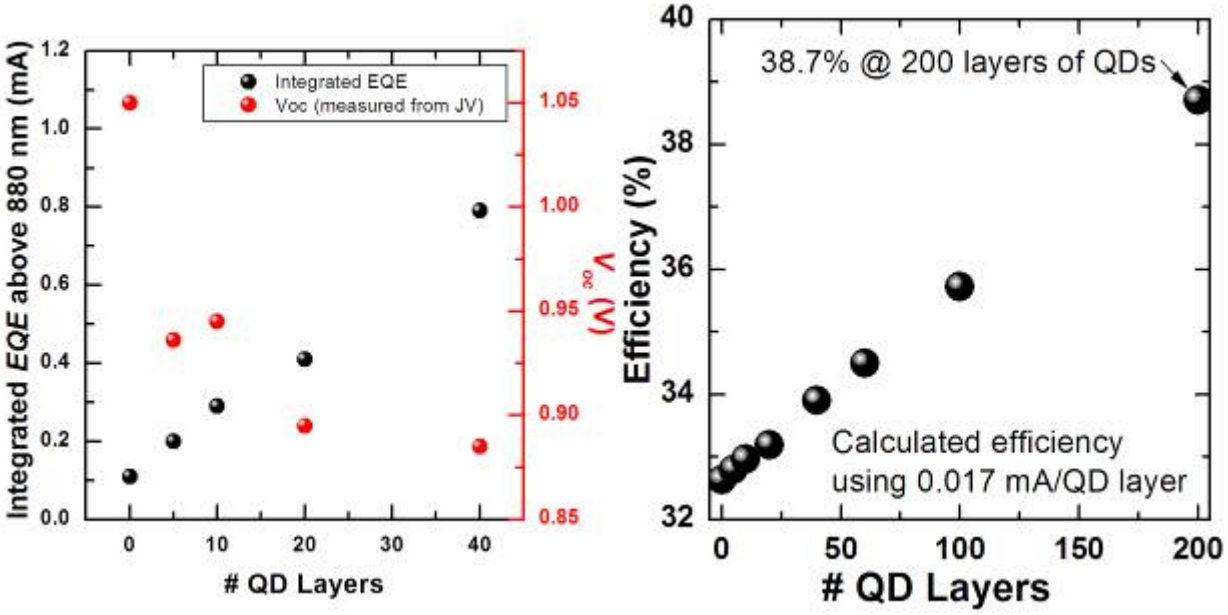

Fig. 21. a) QD contribution to the overall short circuit current, calculated from EQE, as a function of the number of QD layers. Also shows is the measured VOC of each device. b) Calculated TJSC limiting efficiencies with QD bandgap engineering of the middle GaAs junction.

Also shown in Fig. 21a is the measured V_{OC} for the baseline and each QD enhanced cell. The V_{OC} begins to decline with increasing QD layers, however, this decay appears to be saturating at higher numbers of QD layers. The initial decrease in V_{OC} is likely a result of both higher saturation currents and device quasi-Fermi levels equilibrating with the higher energy confined states in the QD region. Therefore, the saturation in V_{OC} reduction with increased QD layers, combined with the steady liner increase in J_{SC}, supports the potential for global efficiency improvements in a triple junction solar cell (TJSC) design.

In order to investigate the potential for global efficiency improvement in the TJSC, detailed balance theory was used to calculate the TJSC limiting efficiency using the values for QD enhancement measured above. Our model without QD enhancement resulted in a limiting efficiency of 32.5% under one sun 6000K blackbody illumination

(see Fig. 21b). This is a widely accepted value for the detailed balance limiting efficiency of a TJSC.

The improvement in a TJSC device with the insertion of QDs into the middle current limiting junction was estimated using detailed balance theory and the 0.017 mA/QD layer increase in J_{SC}. The current of the middle cell was adjusted in the detailed balance model by changing the middle cell bandgap. The middle cell current (and thus bandgap) were adjusted by an amount equal to 0.017 mA times the number of QD layers. The results of this are shown in Fig. 21b. A one sun efficiency of 34.0% is predicted for a 40X QD enhanced TJSC. Increasing the number of QD layers beyond 40X gave 35.7% for a 100X QD enhanced TJSC and 38.7% for a 200X QD cell.

RIT is currently in the process of fabricating and testing a 20X QD enhanced solar cell. Upon completion, this wafer (containing 7 cells) will be delivered to NREL for testing under AM1.5 conditions.

Significant Accomplishments during Phase 2 (post-Go/No-Go) of this project:

1. Growth optimization of InAs QDs on 2" GaAs wafers has resulted in improved uniformity of QD with very low QD coalescence. Standard deviation across a 2" GaAs wafer was reduced by over one order of magnitude using optimized growth conditions. A paper is being prepared for the Journal of Crystal Growth.

2. Demonstrated an open circuit voltage greater than 1.0V with corresponding current enhancement in a QD solar cell. This voltage is the **highest** reported open circuit voltage for a quantum dot solar cell. Results have been reported in the Applied Physics Letters.

3. Demonstrate 40-layer QD solar cell with **absolute efficiency 0.5% greater** than a GaAs control and less then 50mV open circuit voltage loss. This is the first report of both efficiency improvement and low V_{oc} loss in a QD cell and was presented as an invited talk at the IEEE PVSC as well as being published in the IEEE Journal of Photovoltaics.

4. Demonstrate that higher substrate misorientation causes a shift in QD critical thickness for nucleation as well as providing increased QD density and uniformity. This result is a useful guide for both academia and industry, since solar cells are often grown on highly misoriented substrates.

5. CFDRC has implemented a QD solar cell model accounting for both intermediate band levels as well as the QD size effects.

6. Demonstrate growth of uniform InAs QD on large area (4" diameter) GaAs on Ge substrates from Emcore Photovoltaics. Through QD growth optimization, the standard deviation of QD density across a 4" GaAs on Ge wafer was reduced by over one order of magnitude. This result allow larger area and more uniform solar cell results to be obtained.

7. These results lead to the **first demonstration of a dual junction (GaAs on Ge) QD solar cell**. QD dual junction cells show a 0.4 mA/cm^2 current enhancement over the baseline cell.

8. Demonstrate **a triple junction quantum dot solar cell**. Spectral response shows increased sub-bandgap absorption in the middle cell. Integrated current of the (In)GaAs junction with strain balanced InAs QD layers shows a gain of 0.37 mA/cm2 beyond the band edge. One sun current-voltage measurements of QD TJSC show an efficiency of 28.1%, a **0.2% absolute increase** from the baseline.

9. A quantum well solar cell design was developed, grown and tested. Successfully grew and fabricated InGaAs/GaAsP QW solar cells. All cells show sub-bandgap photo-conversion. Under one sun AM1.5 illumination the 10 layer MQW cells show improved short circuit current density (0.5 mA/cm^2).

10. A robust model for the QD solar cell was developed in the physics-based software Crosslight APSYS. This model accurately accounts for QD current enhancement. Model used to predict performance for QD triple junction devices. Model is also being used to study new QD device designs.

Summary of each Task during Phase 2 (post Go/No-Go):

I. **Task 1:** Use metal organic vapor phase epitaxy to grow an array of strain-balanced InAs QDs. Optical characterization (PL), metrology (AFM) and x-ray diffraction (XRD) will be performed as necessary to optimize dot size, dot density and strain. The optimization will draw on previous QD growth results and will yield a uniform array of strain-balanced QDs. The number of stacked QDs will be maximized based on XRD measurements of strain.

In the second phase of this project, this task is separated into two parts. The first was continued growth optimization of QDs on 2" GaAs wafers. The second was optimization of QDs on 4" GaAs on Ge wafers for application in triple junction solar cells (TJSC).

Optimization on 2" GaAs wafers

Optimization of InAs critical coverage is important to realizing controlled growth in quantum dot devices. Substrate misorientation can change the value of critical coverage but also creates more uniform quantum dots in both size and distribution. Uniform quantum dots are advantages in concentrator photovoltaic devices due to increases in sub bandgap response. GaAs *p-i-n* photovoltaic devices were grown via organometallic vapor phase epitaxy and InAs quantum dots using the Stranski-Krastanov growth method on substrates misoriented 6° off (100) in the [110] direction and 2°off (100) in the [110] direction. Both preliminary test and devices structures were created in order to study device performance through electroluminescence, external quantum efficiency, and current-voltage behavior, as well as material properties through atomic force microcopy. Results of this work show that 2° [110] sample results in lower critical coverage as compared to the 6° [110]. Extracted values from the plot shown in Fig. 22 were approximately 1.6 ML verses approximately 1.9 ML for 2° versus 6° offcut, respectively. The 6° [110] substrate also showed a more uniform density and size distribution of QDs (Fig. 22).

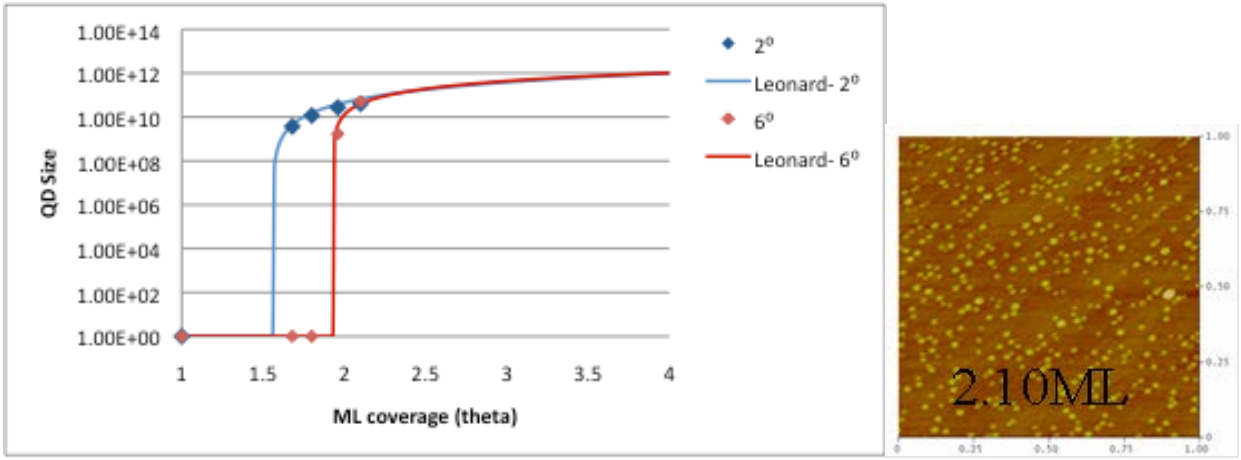

Fig. 22. Plot of QD density versus InAs coverage (left) as well as an AFM micrograph of InAs QD grown on a 6° substrate, showing uniform coverage at 2.1 ML. The solid lines in the plot are a fit to the data used to extract the critical thickness.

Optimization on 4" Ge wafers

Pre-grown GaAs on Ge wafers have been obtained from Emcore Photovoltaics though a collaborative agreement. The wafers include high quality GaAs epilayers grown on thin 150 μm Ge substrates (see Fig. 23). The wafers are a standard 4" diameter, typically employed by Emcore for production of CPV cells. The first goal at RIT is to establish a baseline growth process for InAs QDs on the 4" Ge wafers. In order to do this, a stack of 5 layers of QD was grown on the GaAs-Ge wafers. This stack allows for luminescence spectroscopy to be performed on the QDs. In addition, a single uncapped layer of QDs was grown on top for atomic force microscopy (AFM).

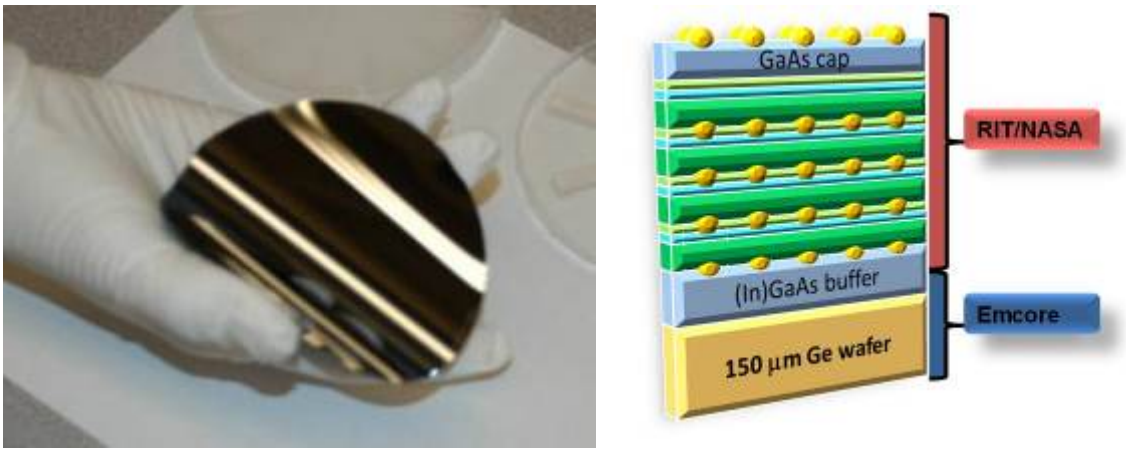

Fig. 23. *a) 150 μm thick 4" GaAs on Ge substrate from Emcore b) test structures grown by RIT on the 4" Emcore wafers.*

Investigations of reactor growth parameters during the InAs QD growth steps were performed in order to study the QD density and uniformity on the 4" GaAs on Ge wafers. Higher temperature, balanced injector flow, and higher chamber pressure trend toward improved uniformity, as measured based upon the standard deviation (σ) of the QD density across the surface of the wafers. An increase to 70 Torr provided an increase in QD across-wafer density uniformity (from a standard deviation of 1.5 x 10^{10} to 6.0 x 10^{9}). Balancing the alkyl injector flow rates was also studied as a factor for the overall improvement of QD density. Shifting 50 sccm of the alkyl flow rate from the outer to the inner injector provided an increase in QD density uniformity while maintaining a high QD density. Increasing temperature decreases the overall density but improves the uniformity, as seen in Fig. 24.

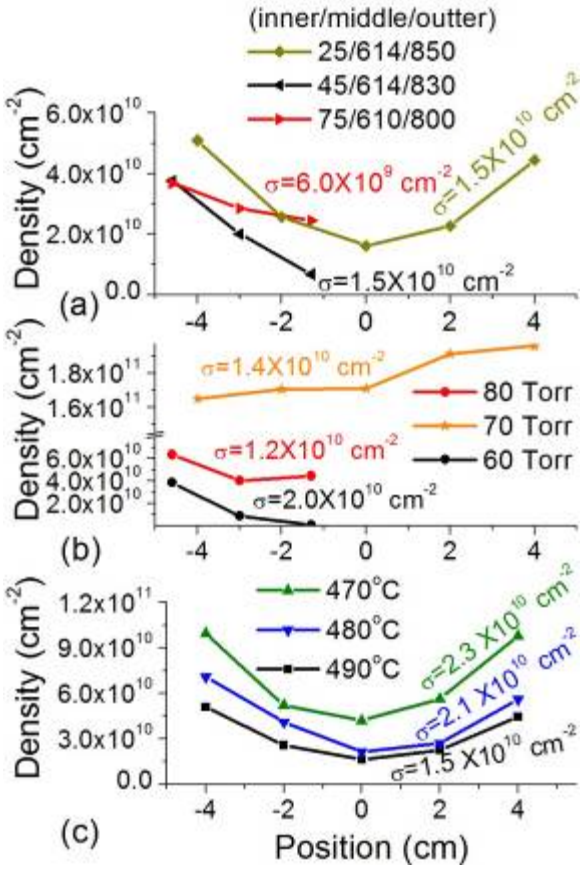

Fig. 24. Variation of QD density across the 4" wafer for different growth conditions(a) increasing the flow rate to the inner injector has negligible change; (b) higher chamber pressure increases QD density and decreases σ; (c) higher temperature decreases QD density but leads to a lower standard deviation (σ).

A series of QD samples were grown with varying InAs growth times (coverage). As can be seen below in Fig. 25, the QD do not begin to nucleate until 11s and QD ripening begins to occur at 14s and beyond. A plot of the QD density and PL intensity is shown in Fig. 26. Critical thickness is near 10.5s of InAs growth. The onset of ripening correlates with reduction in optical intensity (i.e. defective QDs begin to form). The QD uniformity across the 4" wafer is shown in Fig. 25 (70 Torr curve). Denisty is maintained above 1x10^{11} cm^{-2} with a standard deviation similar to that seen on 2" wafers.

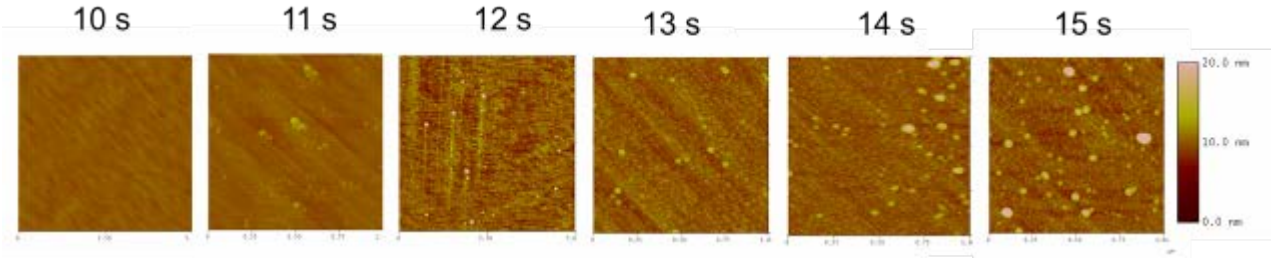

Fig. 25. AFM images of QD formation on 4" GaAs on Ge wafers as a function of InAs coverage.

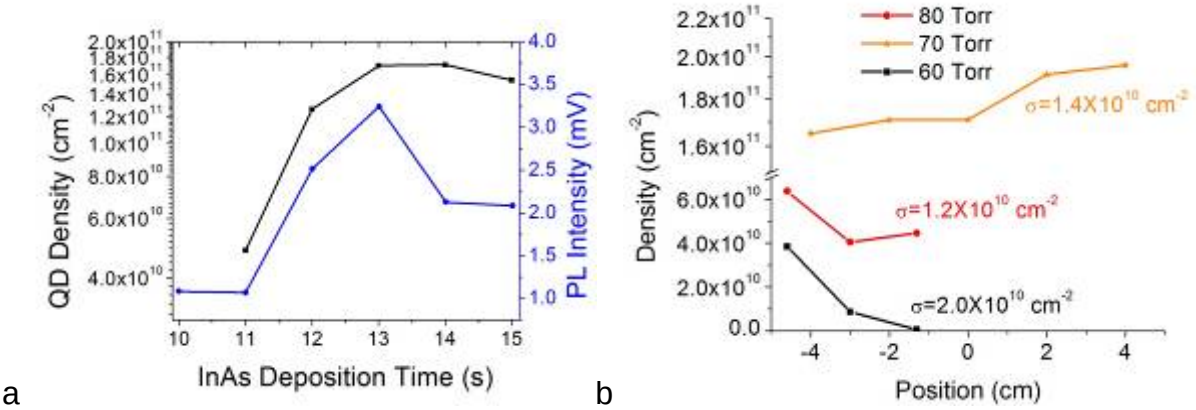

Fig. 26. a) Plot of QD density (left axis) and QD PL intensity (right axis) as a function of InAs coverage b) QD density as a function of potions across the 4" GaAs on Ge wafer (70 Torr curve).

II. **<u>Task 2.</u>** Growth of baseline and strain-balanced QD enhanced single junction GaAs pin solar cells. QDs will initially be embedded in the i-region of the cell. Cells will be characterized under one-sun Air Mass 1.5 conditions. Efficiency and related metrics will be measured. Characterization of the cells under concentration will be performed in order to gauge how QD cells efficiency, short circuit current and open circuit voltage are affected by high concentration conditions. Cell optimization will be performed as needed to improve cell performance under concentration.

Offcut Study

As was shown in Task1 above, growth of QDs on miscut substrates show that 2° [110] samples results in a lower critical coverage for QD formation as compared to the 6° [110]. Standard pin solar cells were grown on both 2° and 6° substrates. Fig. 27a shows the 1-sun light IV response of the 2° 1.80 ML case and the 6° 2.10 ML case. These samples were chosen for comparison because they are representative of the maximum thickness before the onset of Ostwald ripening. Baseline results show a standard GaAs cell with no QDs grown on a 2° substrate. It is clear that the QD devices (both 2° and 6°) show enhancement in current. The 6° sample displays the most current

gain with an J_{sc} of 24.5 mA/cm^2 while the 2° sample had an J_{sc} of 23.18 mA/cm^2. This is an improvement in the 6° sample over the baseline of 1.3 mA/cm2. These results can be compared to the QD densities shown in Task 1. The highest QD density produced the highest Isc. Table 4 shows a summary of device results.

Table 4. Extracted one sun solar cell parameters for a baseline cell without QDs and 10 layer QD cells grown on 2° and 6° offcut substrates.

Device	I_{sc} (mA/cm^2)	V_{oc} (V)	Efficiency (%)	Fill Factor (%)
Baseline	22.77	1.06	14.54	81.89
2° 1.8 ML	23.18	1.00	12.63	74.00
6° 2.1 ML	24.50	0.95	13.71	80.31

The spectral responsivity is shown in Fig. 27b. It is clear that in the sub-bandgap region, the QD devices are performing equivalently. Wavelengths above the GaAs band edge (~870 nm) show enhanced current collection, which can be seen in the inlay in Fig. 27b. The 2° 2.10 ML sample shows similar QD response as compared to the 6° 2.10 ML response. Since QD density was optimized on both substrates, the high quality of QDs leads to equivalent absorption profiles on both 2° and 6° substrates.

Overall, these results, show that short circuit current enhancement is possible in a variety of offcut substrates as long as the critical thickness of QD formation is characterized. This is an important result since commercial cell manufactures often use large area (4" diameter) as well as highly vicinal (2-11° offcut) substrates.

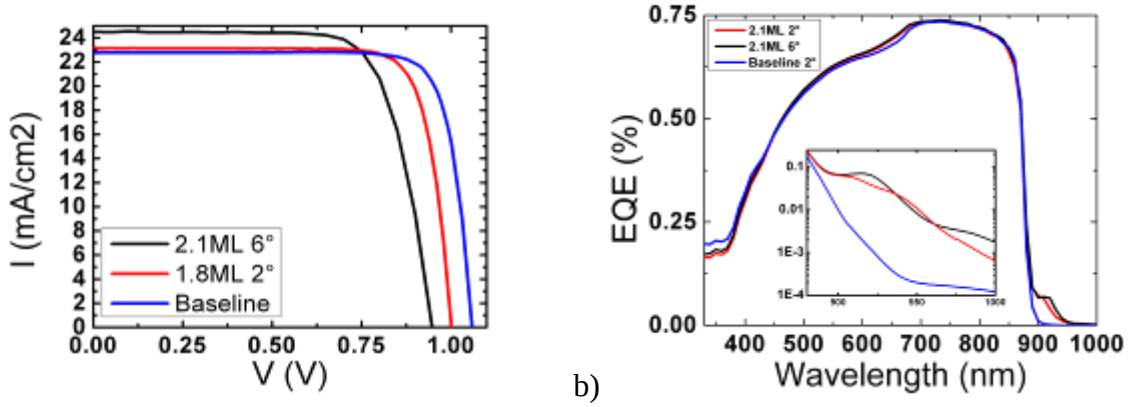

a) b)

Fig. 27. a) One sun illuminated JV curves for a baseline cell without QDs and 10 layer QD cells grown on 2° and 6° offcut substrates. b) spectral response of the baseline cell compared to the two QD cells on various offcut substrates.

Improving QD absorption

Solar cells with 10, 20, and 40 layers of QDs have been grown using the optimized InAs surface coverage as described in Phase 1 (pre go/no-go). The 10 and 20 layer devices have demonstrated improved current generation over baseline devices without QDs, as well as comparable current gain from integrated QD response to the non-

optimized InAs coverage. The improved InAs coverage has also lead to a continued increase in open circuit voltage as compared to the non-optimized InAs coverage devices. One sun light IV as well as spectral responses are shown below in Fig. 28.

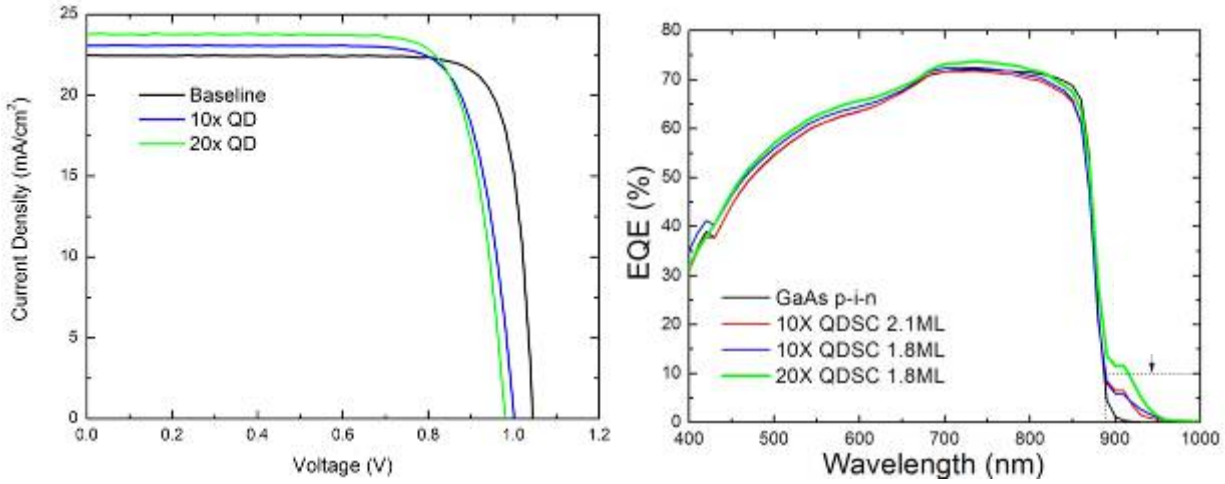

Fig. 28.. a) One sun light IV for baseline and 10-20 layer QD solar cells b) externals quantum efficiency show the sub-bandgap response region.

Ten, twenty, and forty-layer InAs/GaAs quantum dot (QD) embedded superlattice solar cells were compared to a baseline GaAs *p-i-n* solar cell. Proper strain balancing and a reduction of InAs coverage value in the superlattice region of the QD embedded devices enabled the systematic increase in short circuit current density (see Fig. 29) with QD layers (0.02 mA/cm^2/QD layer) with minimal open circuit voltage loss (~50 mV). The improvement in voltage was found to be due to a reduced non-radiative recombination resulting from a reduced density of larger defective QDs and effective strain management. The forty layer device exceeded the baseline GaAs cell by 0.5% absolute efficiency improving efficiency relative to the baseline by 3.6%. Results have been reported in two recent publication in the Applied Physics Letters as well as the IEEE Journal of Photovoltaics.

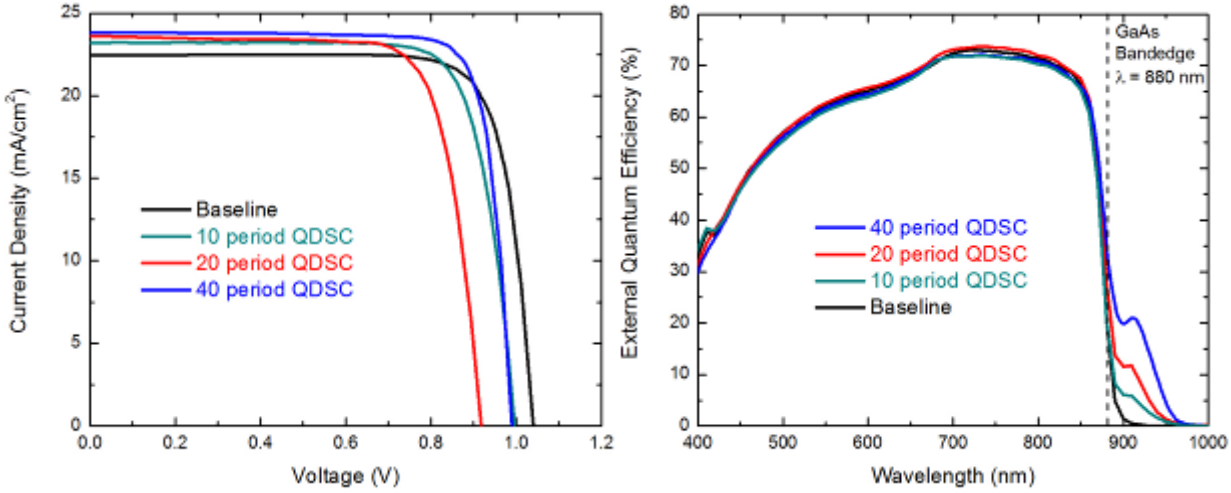

Fig. 29. a) Illuminated 1-sun J-V curves for the three QD and the baseline/control GaAs p-i-n solar cell devices, indicating a clear increase in short circuit current density and minimal loss in open circuit voltage for the 10- and 40-layer QD cells. b) External quantum efficiency measurements for the three QD and the baseline/control GaAs p-i-n solar cell devices, indicating no significant degradation in the bulk GaAs absorption wavelengths and a consistent increase in sub-GaAs bandedge EQE values with increasing numbers of QD layers.

III. **Task 3.** Initial models for QD enhanced solar cells will be developed using the CFD Research Corporation modeling suite and compared to our above experimental results. In order to confirm model, standard GaAs pin solar cells (w/o QD) will also be modeled and compared to experimental results for our baseline cells.

This task was fully completed in Phase I of the project. Further modeling work was done under Task 6 and Task 11.

IV. **Task 4.** Measure the dark and light (AM1.5) current versus voltage behavior and the spectral response of GaAs-based pin solar cells with and without an InAs quantum dot array in the intrinsic region as functions of temperature. Temperature coefficients will be determined for QD enhanced GaAs pin solar cells. Thermal conductivity and behavior will be both experimentally and theoretically analyzed with the goal to predict and enhance operation of the QD cell under concentration and high temperature conditions.

The majority of this task was completed in Phase 1 of the project. However, during Phase 2 we also explored thermal activation energy of the QD solar cells. Solar cell processes involves both the photon generation of electron hole pairs, as well as collection at their respective potential. In order to isolate these two processes, it is important to optically characterize these devices. For the quantitative investigation of the carrier dynamics, rearrangement of the standard PL rate equations can yeild:

$$I(T) = \frac{P}{1 + \left(R'/U\right) + \left(R'/R\right)e^{-E_a/kT}}$$

where the ratio R'/R is of importance as an extractable parameter representing the ratio of non-radiative to radiative recombination. In addition, E_a, is representative of the activation energy in an Arrhenius relationship. In QWs and QD systems, this often represents the energy barrier seen by a trapped carrier, and is closely related to the difference in energy from the top of the barrier conduction band to the energy state of the carrier. Plotted in Fig. 30 (left), the data for the 1.82ML sample is shown and a fit to extract activation energy and the recombination parameter. In this Fig., the dotted lines fit to four data points each indicating the dominant temperature regions of each state. Activation energies and recombination constants are extracted from each fit.

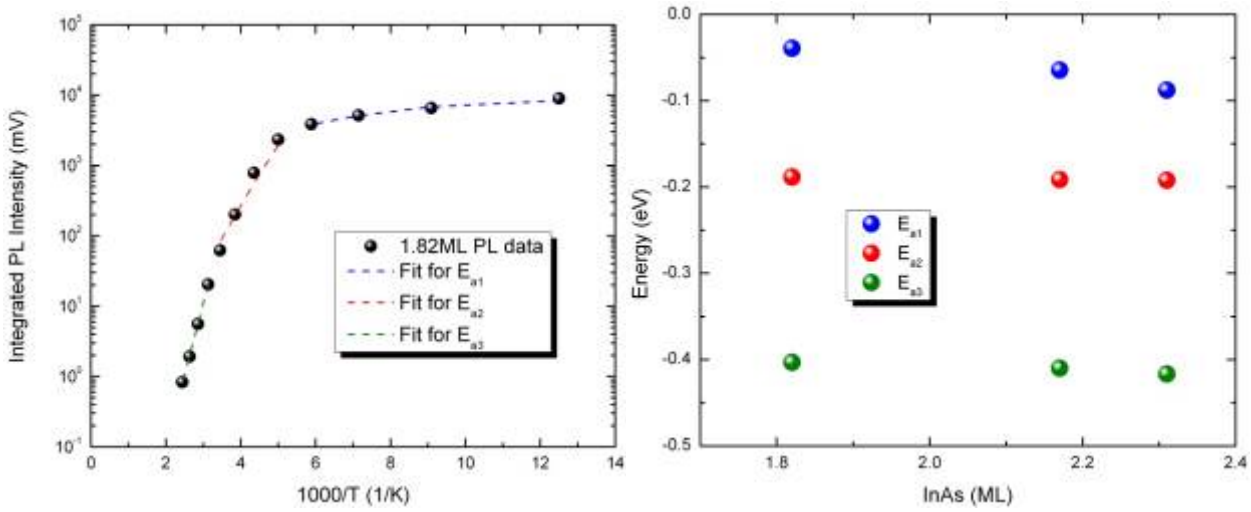

Fig. 30. a) Integrated PL intensity of the sample vs. temperature and the corresponding fit. b) extracted activation energies are plotted here versus InAs coverage value.

Fig. 30 (right) illustrates the states obtained from the parameter extraction for all InAs coverage samples. The most obvious feature in Fig. 30 is that the top most, or closest to the conduction band state decreases with increasing InAs coverage. This correlates with quantum mechanical theory and the state value corresponds with accepted literature value range of the WL state (1.25-1.35 eV). The two states below suggest QD states at values of roughly 200 and 400meV below the conduction band. These values appear to be relatively insensitive to the varying InAs coverage. The recombination parameter R'/R, not shown, stays relatively constant for the QD states, but shows a significant shift upwards with increasing Θ_c. This indicates that the sample with the lowest number of larger quantum dots and lowest InAs coverage has the most efficient radiative recombination of all of the samples. With the improvement of optical quality and the reduction in non-radiative recombination, quantum efficiency can be improved and higher current values may be available for collection from the QD structures. Results from 3 above indicate just this effect, that lower InAs coverage leads to improved QD uniformity and coalescence, thus giving improved values of Jsc and Voc compared to higher InAs coverage. The improved accuracy of the strain compensation associated with a monodisperse QD distribution may also improve the ability to increase the number of these layers available for i-region insertion. This would increase the absorption cross section of the lower-bandgap material, contributing further to the current.

V. **Task 5**: Use in-line atmospheric attenuation filters to measure performance and spectral response of cells as a function of changing atmospheric conditions. This will be done using both a baseline SJ GaAs cell, a QD enhanced GaAs cell and a full commercially produced triple-junction baseline.

In this task, spectral mismatch was calculated for a number of solar cell types under both AM0 and AM1.5 illumination. Spectral mismatch allows for evaluation of a spectrum based on the spectral responsivity of an actual device. Specifically, these factors evaluate deviation in the simulated spectrum from the reference spectrum based on the spectral responsivity of the cell used for calibration and the cell under test [5]. This provides a figure of merit for confidence in cell measurements when a closely matched calibration standard is not available, as is often the case for non-standard cells such as those integrating quantum confined structures or novel material systems. Spectral mismatch, *M*, was calculated for several material systems or cell designs using the equation below.

$$M = \frac{\int_{\lambda_l}^{\lambda_u} E_{SIM}(\lambda) SR^{TEST}(\lambda) d\lambda \int_{\lambda_l}^{\lambda_u} E_{REF}(\lambda) SR^{CAL}(\lambda) d\lambda}{\int_{\lambda_l}^{\lambda_u} E_{REF}(\lambda) SR^{TEST}(\lambda) d\lambda \int_{\lambda_l}^{\lambda_u} E_{SIM}(\lambda) SR^{CAL}(\lambda) d\lambda}$$

where λ_u and λ_l represent the upper and lower bounds of pertinent wavelengths, E_{SIM} is the spectrum of the simulator, E_{REF} is the reference spectrum (AM0, etc.), SR^{TEST} is the spectral responsivity of the device under test, and SR^{CAL} is the spectral responsivity of the cell used to calibrate the simulator [5]. The external quantum efficiencies of the three sub-cells primarily used to calibrate the simulator to AM0, as well as calculate spectral mismatch, can be seen in Fig. 31.

Once calculated, the mismatch factor can be used to adjust the I_{SC} measured under simulated conditions to a more realistic I_{SC} under a reference spectrum using equation 3, where *I* is I_{SC}, the superscript denotes the cell under test or the calibration cell, and the subscript denotes whether the I_{SC} was measured under the reference or the simulated spectrum.

$$I_{REF}^{TEST} = \frac{I_{SIM}^{TEST}}{M} \frac{I_{REF}^{CAL}}{I_{SIM}^{CAL}}$$

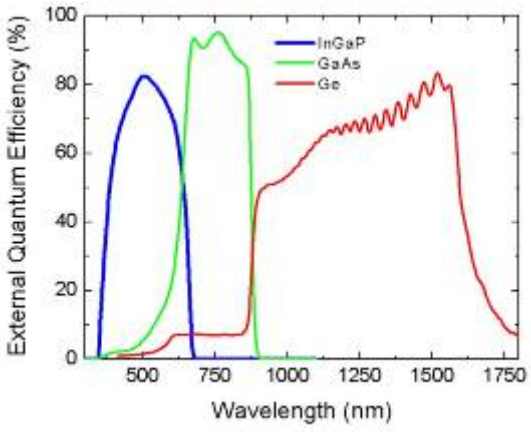

Fig. 31. External quantum efficiency of the International Measurement Round Robin cells used to calibrate the simulator.

Table 5 shows several spectral mismatch factors calculated using both the InGaP and GaAs calibration cells under simulated AM0 and AM1.5G spectra. Additional cells were selected to represent a range of devices typically measured on the tool, and are described presently. MQW: a GaAs single junction cell with 10 repeat units of a $In_{0.17}Ga_{0.83}As/Ga_{0.94}As_{0.06}P$ multiple quantum well (MQW); QD: a GaAs solar cell with 60 repeat units of InAs quantum dots strain compensated with GaP; GaP: a single junction GaP solar cell (E_G = 2.78 eV); GaAs: a single junction GaAs cell; InGaP: a single junction InGaP cell.

Table 5: Spectral mismatch factor for various cell types as a function of calibration cell, for both AM0 and AM1.5G.

AM0	**MQW**	**QD**	**GaP**	**GaAs**	**InGaP**
InGaP	1.12	1.15	0.967	1.11	1.02
GaAs	0.938	0.962	0.810	0.932	0.857

AM1.5G	**MQW**	**QD**	**GaP**	**GaAs**	**InGaP**
InGaP	1.05	1.07	0.848	1.04	1.01
GaAs	0.987	1.01	0.798	0.979	0.952

In instances where a calibration cell and cell under test have a nearly identical bandgap and spectral responsivity (such as the InGaP/InGaP pairing) the *M* value is nearly unity, as would be expected. In the case of the GaAs/GaAs pairing, the GaAs component cell has a narrowed spectral response range as compared to the single junction GaAs cell due to its InGaP window. In most cases, when calibration cells are chosen as close to the bandgap of the material, the value of *M* is close enough to unity to modify I_{SC} by less than 5%, assuming a negligible difference in the I_{SC} of the calibration cell under the simulated spectrum. Spectral mismatch adjustments to I_{SC} would, in the best case in Table 2 (GaAs/QD under AM1.5G), decrease a cells I_{SC} by 0.99%, while the worst case (GaAs/GaP under AM1.5G) would decrease I_{SC} by 25%.

VI. Task 6: Initial numerical models will be used in conjunction with previous results to develop QD enhanced pin solar cell numerical models. Based on these model results we will further optimize our device structure (QD size, density, stacking, layer thickness, etc.) for high concentration conditions.

CFDRC Activity

To demonstrate the effect that quantum dots can potentially have on the efficiency of a p-i-n solar cell, a detailed balance model of a single junction Intermediate Band Solar Cell (IBSC) was made using the method of Lagrange Multipliers. These

methods were used in order to accurately and quickly calculate the efficiency of an IBSC. The standard band diagram of the IBSC is shown in Fig. 32. The intermediate band which is formed by a quantum dot array makes it possible for lower energy photons to be absorbed thus expanding the absorbed spectral range. This can theoretically increase the solar cell's efficiency. Fig. 33 shows the efficiency results of the detailed balance simulation under a 6000K black body spectrum at one-sun and full concentration. Also presented are the efficiencies of single junction solar cells with the same material band gaps, but without an intermediate band (no quantum dots).

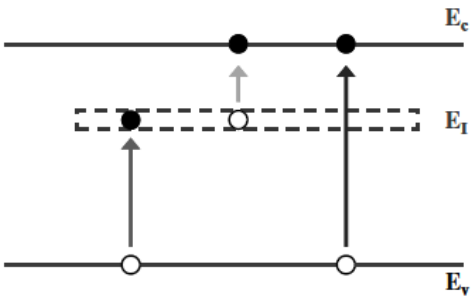

Fig. 32. Band diagram of IBSC. Shows electron energy transitions from Ec to Ev excited by a photon of energy equal to or greater than Ecv. Similar transitions are shown for energy transitions of Ev to Ei and Ei to Ec.

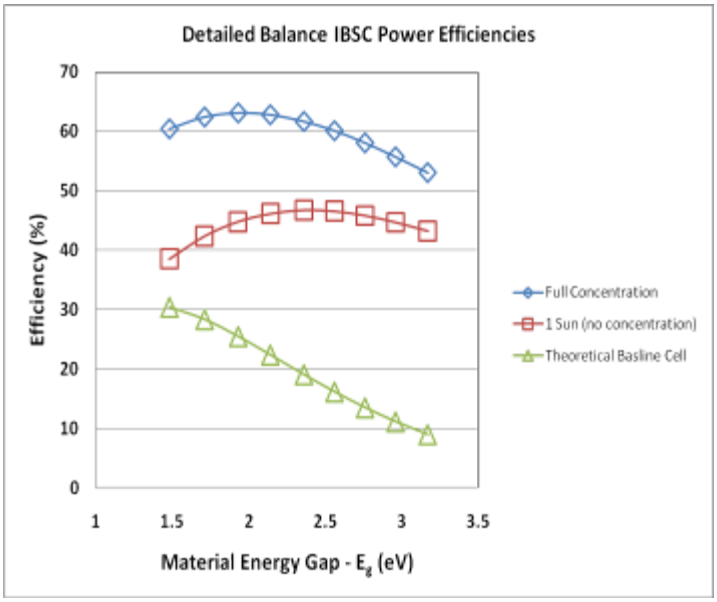

Fig. 33. Results of detailed balance simulation of IBSC at one-sun and full concentration. Single-junction cell efficiencies are shown for comparison at the respective material band gaps.

It is clear from Fig. 33 that with the introduction of an intermediate band through the use of quantum dots, the efficiency of a single junction solar cell can be dramatically increased. For a more physical and well known example, consider the InAs/GaAs

(dot/host) system. This system has Eci and Eiv values of approximately 0.4 eV and 1 eV respectively. Using these values, our detailed balance model gives a maximum efficiency of 36.6%. This is a notable increase from the theoretical maximum efficiency of 31% for a single junction GaAs baseline cell.

One of the most appealing features exhibited by quantum dots is the ability to tune their spectral absorption range based on the size of the dots. This feature is demonstrated in Fig. 34. This characteristic of quantum dots is what makes their marriage with the p-i-n device so promising.

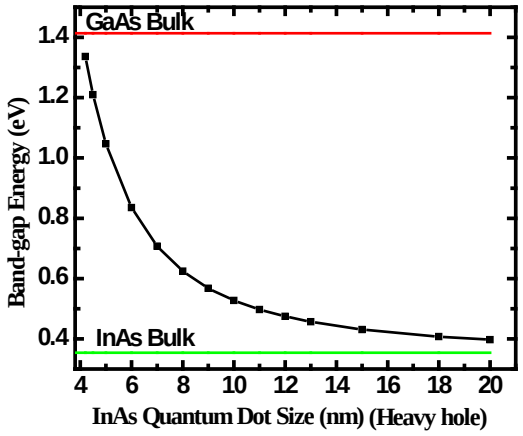

Fig. 34. Effective band gaps of QD layers as a function of QD size.

In theory, one could grow quantum dots of various sizes. This could spread the absorption range of the p-i-n device considerably. In addition to increased absorption, one would also have increased radiation tolerance brought on by the radiation harness of the quantum dots and the long life times exhibited by the p-i-n structure.

RIT Activity

The incorporation of nanostructures, such as quantum dots (QD), into the intrinsic region of III-V solar cells has been proposed as a potential route towards boosting conversion efficiencies with immediate applications in concentrator photovoltaic and space power systems. Through the careful selection of nanoscale materials and geometries it is possible to engineer the active material bandgaps of intermediate-band and multi-junction solar cells and optimize the collected light that is converted into useable electrical power. Necessary to the optimization process of this particular class of solar cells is the ability to correlate nanoscale properties with macroscopic device characteristics. To this purpose, we have developed a modeling routine using the physics based software Crosslight APSYS to systematically study how the inclusion of embedded quantum structures influence the performance of photovoltaics. Crosslight APSYS is a general purpose 2D finite-element analysis and modeling software program designed for compound semiconductor devices based on the drift-diffusion model. In addition, and unique to this platform, is the ability to model quantum confinement effects (which arise when nanoscale layers are implemented) with an intrinsic Schrödinger

solver. In particular, this tool is applied to study how nanoscale variables, including size, shape and material compositions, alter the electrical and optical properties at the device level. In addition, macro-level engineering of the nanostructures, such as the number of stacked layers as well as the position of these structures within the device, is explored in optimizing the overall device response

As a preliminary step, the program was used to predict the performance of a single-junction *pin*-GaAs solar cell which will serve as the baseline for subsequent studies. As shown in Fig. 35, the simulation results agree well with measured data from an actual device with calculated values for V_{OC}, J_{SC}, fill factor and power conversion efficiency of 1.034 V, 22.49 mA/cm^2, 80.12% and 13.64%, respectively and include all major loss mechanisms including spectral reflection and carrier recombination. The material parameters employed are taken from widely accepted databases based on measurements and physical models. It is worth noting that no anti-reflection coatings were used in order to focus solely on the change in device performance due to the embedded nanostructures. In parallel, the quantum module was used to calculate the band structure and absorption of a multi-layer stack of InAs QDs embedded in GaAs. For this investigation a truncated pyramid with a height (base) of 3.5 nm (20 nm) was selected to best describe the physical system. In addition, a thin layer of InGaAs (0.5 nm) has been included in the quantum solver to take into account absorption due to wetting layer states and a QD surface density of 1x10^{10}cm^{-2} assumed. Within the software it is possible to incorporate the outputs of the quantum solver, including bound energy state levels and optical transition strengths, as parameters of the active region of the device. This technique enables full characterization of the nanostructured device and has been used to explore a range of devices with various geometries.

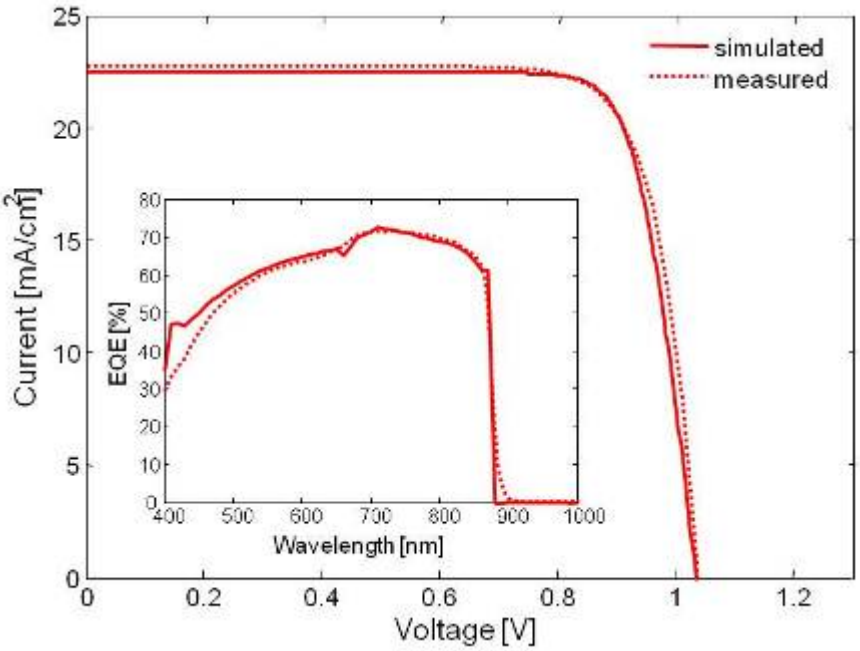

Fig. 35. Simulated (solid) and measured (dotted) current-voltage characteristics for a *pin*-GaAs solar cell. The inset shows the external quantum efficiency spectra.

Results:

5X QD single junction

The simulation results based upon the two-step process described are depicted in Fig. 36 for a baseline and a nanostructured *pin*-GaAs solar cell. In this case, a 5 layer superlattice of uncoupled InAs QDs was centered in the intrinsic region of a *pin*-GaAs cell. For comparison, the active region in both devices was kept constant at 100 nm and all simulations were performed under AM0 conditions. The enhancement in performance offered by the incorporation of QDs is clearly visible in the external quantum efficiency spectrum where sub-bandgap absorption is observed at wavelengths above 880 nm. Two prominent peaks predicted at 940 and 1060 nm can be ascribed to transitions between confined stated of the wetting layer and QD, respectively. Based upon the integrated quantum efficiency above 880 nm, our model predicts a short-circuit current enhancement of 0.072 mA/cm^2.

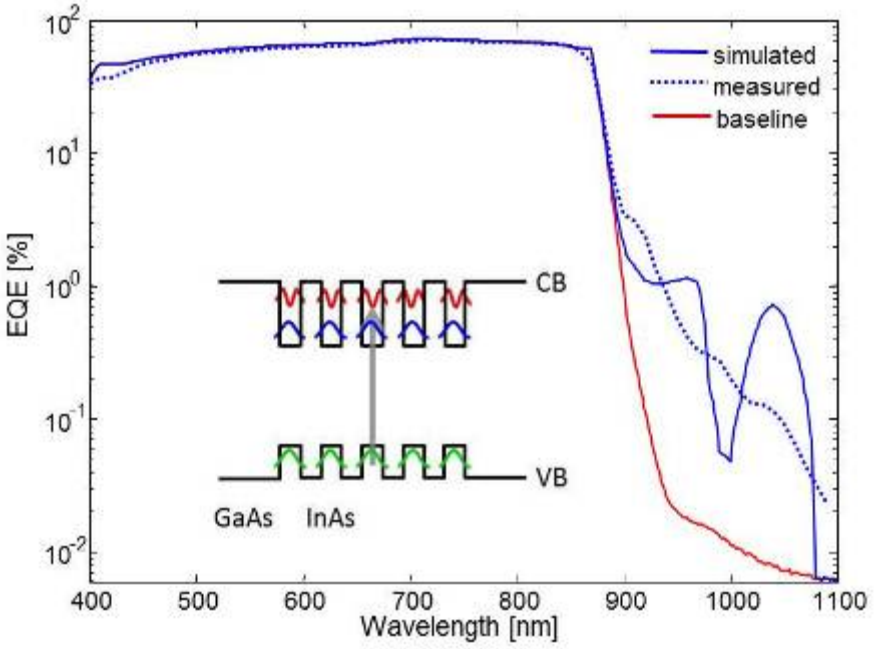

Fig. 36. External quantum efficiency versus wavelength simulated for a *pin*-GaAs solar cell with (blue) and without (red) quantum dots. For comparison representative data from a nanostructured device is also included (blue dotted). The inset depicts the electronic structure of a GaAs solar cell embedded with InAs quantum dots.

For comparison, representative data from a previously fabricated 5-layer QD solar cell is also included in Fig. 36 which shows a reasonable correlation between the simulated and experimental results. Here, the integrated measured spectral response above 880 nm yields a 0.092 mA/cm^2 increase in photocurrent. While this is fairly close to the simulation prediction, the discrepancies likely originate from the evident mismatch

between the quantum efficiencies observed and predicted. For example, the model simultaneously overestimates the contribution from the QD and underestimates the influence of the wetting layer. In addition there is a notable shift in where these features lie spectrally. As this sub-bandgap contribution to the photocurrent is directly related to the electronic structure of the embedded QDs, it is clear that the quantum model must be further modified to ensure a more accurate representation. One possible source of error is the calculation of the strain distribution within the nanostructure which greatly affects band offsets and confined state levels through the deformation potential. The current software neglects the three-dimensional nature of the strain distribution which gives rise to these discrepancies in transition energies. Although this approach remains suitable for the purpose of predicting trends at the device level, efforts are underway to improve the accuracy of the quantum model using external software such as *nextnano*[3]. We are continuing to improve our simulation capability through new funding from the DoE Next Generation II program with UCLA.

Layer number study

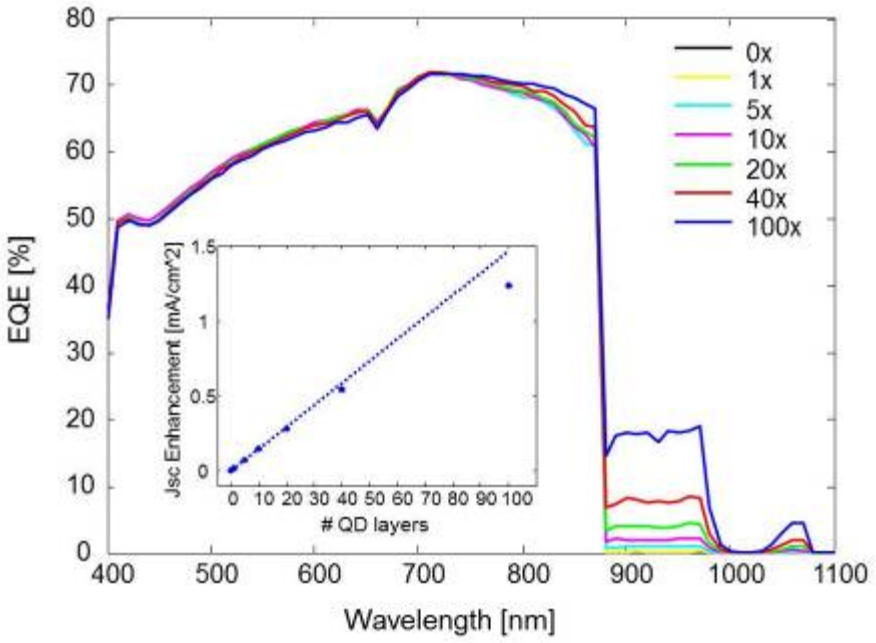

Fig. 37. External quantum efficiency versus wavelength simulated for a *pin*-GaAs solar cell as a function of the number of embedded QD layers. The inset depicts the enhancement in short-circuit current density with increasing number of QD layers.

A series of simulations were run where the number of QD layers varied from 0 to 100 to investigate the effect of the number of embedded nanoscale layers on the overall device performance. The results of this series, quantum efficiency plots and the corresponding sub-bandgap integrated photocurrent, are illustrated in Fig. 37. With the addition of more QD layers, the sub-bandgap quantum efficiency increases

monotonically with negligible change in the bulk response, even up to 100 layers. In fact, in the many layer structures, there is a slight increase in the GaAs response at the band-edge due to the significantly larger volume of bulk material in these devices. This is a significant result as it implies that (in the absence of the material degradation typically associated with such a larger number of QDs) carrier collection is still efficient in active regions exceeding 1 µm. In fact, up to 20-layer QDs the short-circuit current enhancement is linear with a predicted enhancement of 0.0149 mA/cm2/layer. This is in good agreement with previous studies which observed up to a 0.02 mA/cm2/layer linear increase in the sub-bandgap photoresponse. Beyond 20-layers the sub-bandgap response begins to deviate from this linear trend suggesting a saturation of the QD response, possibly due to an optical depth limit as the intrinsic region becomes exceedingly thick. In this case, beyond a critical number of layers, the sub-bandgap light is completely absorbed by the QDs so that the addition of more nanostructures no longer provides an appreciable enhancement in the photocurrent. To validate this, test structures with varying number of QD layers will be grown to determine the experimental QD absorption cross section. This is being continued under the DoE Next Generation II program with UCLA.

Position-dependent study

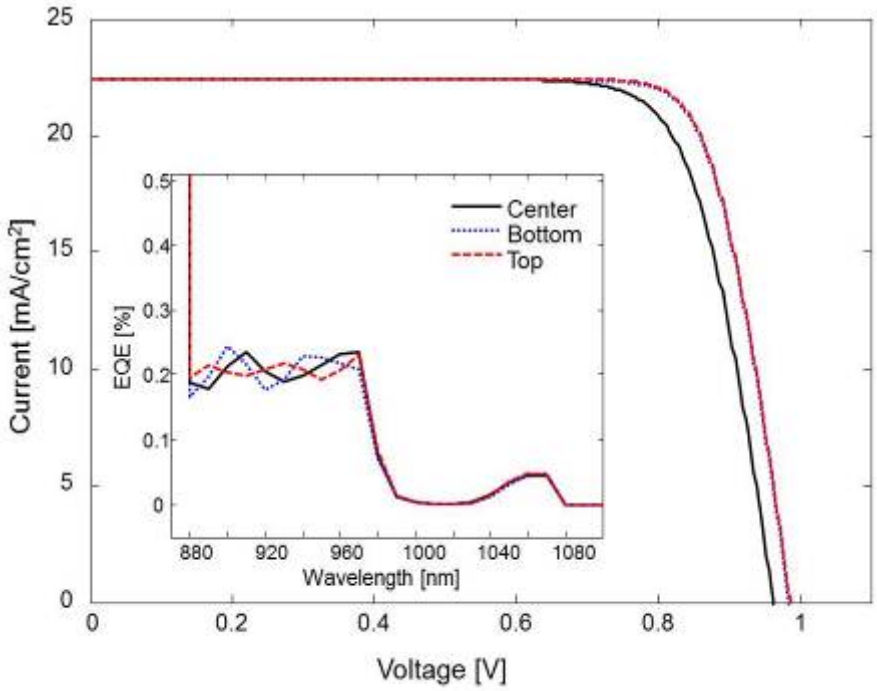

Fig. 38. Current-voltage characteristics for a *pin*-GaAs solar cell for various position of a single QD layer. The inset depicts the associated external quantum efficiency sub-bandgap spectra.

The effect of the placement of the nanostructures within the intrinsic region on device performance was also considered. Devices were simulated which contained a single quantum dot located near the *n*-doped edge, in the exact middle and near the *p*-

doped edge. As depicted in Fig. 38, external quantum efficiency simulations show spectral variations in the wetting layer contributions from the QDs at the different locations. Since the electronic structure of the wetting layer is calculated at the device level, this difference is attributed to local field induced shifts in the electronic states. As expected, the J_{sc} is nearly identical for the three positions as all are located in a high field region and charge collection at short-circuit remains efficient. However, the current-voltage scans reveal an additional loss of 20 mV for the QD located in the exact center of the intrinsic region versus those located near the doped edges. This result is consistent with theoretical predictions of QW solar cell device performance. Non-radiative recombination, the dominant loss mechanism in nanostructured solar cells, is greatest in the middle of the intrinsic region where the electron-hole density product is maximized. Thus, in order to optimize the enhancement offered by the QDs it is necessary to strategically place them off-center in the intrinsic region where non-radiative recombination rates are expected to be lower. This effect becomes increasingly significant when designing structures which utilize only a few layers of QDs. To further explore this finding, a series of three samples with the 5 layer superlattice of QDs placed in the center and near the doped regions of a *pin*-GaAs solar cell have been grown using MOCVD with device fabrication and full characterization underway. This is being continued under the DoE Next Generation II program with UCLA.

VII. Task 7: Development of tunnel junctions suitable for use under the optimal concentration conditions measured in Period 1. This tunnel junction is a critical link between the top and bottom cell in the tandem structure.

Two tunnel junction have been designed, grown, fabricated, and tested. The basic design structure for both is shown below in Fig. 39. Current-voltage characteristics of these designs can be seen in Fig. 40a. The first, an n/p design, achieved a peak current density of 589A/cm², and a peak to valley ratio (PVR) of 20.06. The specific resistance of the negative differential resistance region (NDR) was 3.39×10^{-4} Ωcm^2. The second design incorporated a thin intrinsic region at the metallurgical junction, with promising results. This n/i/p device produced a larger peak current density of 1891A/cm² and an improved PVR of 20.12. Additionally, the specific resistance of the NDR was reduced to 1.54×10^{-4} Ωcm^2. The addition of the i-region separator had a clear impact on dopant diffusion across the junction, leading to the improved results. This n-i-p design is sufficient for one sun tandem cells with current density of 17-20 mA/cm^2. However, further optimization would be necessary for high concentration tandem cells where current density can exceed 6-8 A/cm^2.

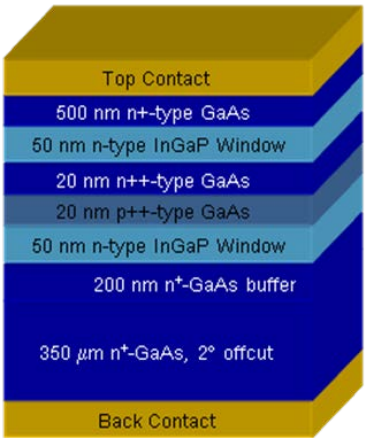

Fig. 39.. Tunnel junction test structure.

Work was also done on numerical modeling of these structures using the Sentaurus software package by Synopsys. Early I-V results of a simplified GaAs tunnel diode, seen in Fig. 40b, show working simulation of tunneling-induced NDR. At this stage of development, the current density is unreasonably low and the PVR is unreasonably large for this material system. Improving the definitions of GaAs material properties within the software to more realistic values measured in-house should greatly improve the quality of this simulation.

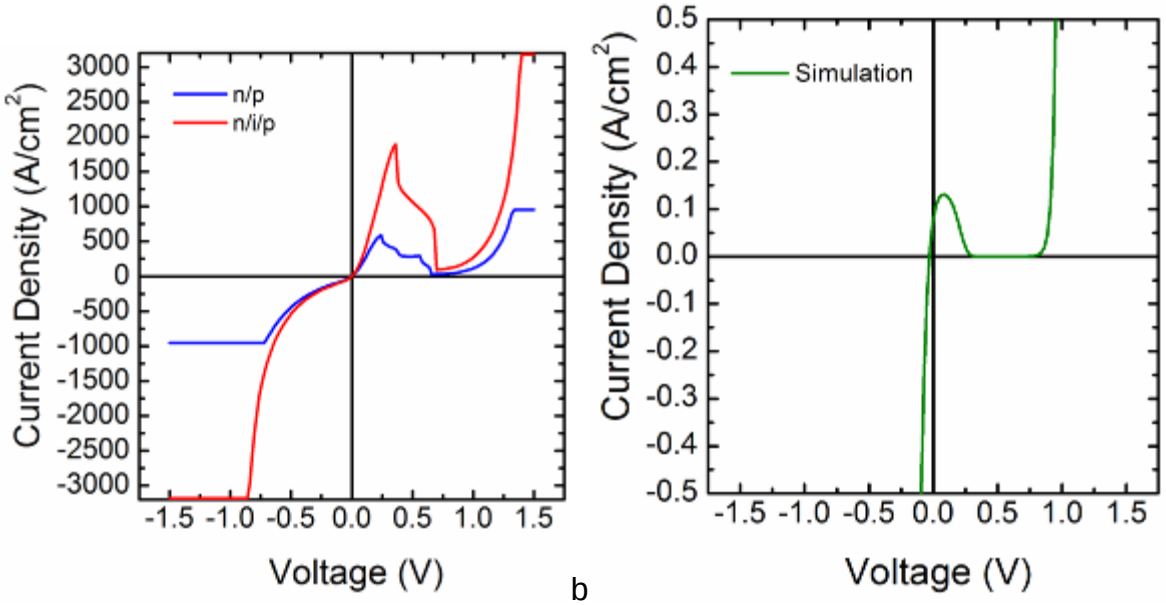

Fig. 40. a) Tunnel junction current density versus voltage curves showing NDR and high peak current b) simulated tunnel junction current density curve.

VIII. Task 8: Growth of a baseline and QD enhanced tandem InGaP/GaAs cell. Device structures will be fabricated and characterized, with emphasis on concentration. The thermal coefficients and sensitivity to spectral conditions will be analyzed. Device design optimization based on experiment as needed for operation under concentration. Numerical models will be extended to include tandem InGaP/GaAs cell with QD enhancement in the GaAs region. Design will be optimized for concentration conditions, such that the model device will have optimal efficiency at elevated temperature and under variable spectral conditions.

Rather than focusing on the top-middle cell combination, we have instead collaborated with Emcore to growth at middle-bottom cell device with QDs. In Task 11, this was inserted into a full triple junction by growth the top InGaP layers. In addition, thermal and concentration effects were studied under Task 11 rather than in this task.

Double junction GaAs/Ge solar cells are fabricated with and without QDs in the GaAs junction. The structure of the double junction solar cells is shown in Fig. 41. The sub-band gap current generation in the GaAs top junction can be seen in Fig. 42. The per layer current contribution of the QDs is 0.2 mA/cm^2 as determined by subtracting the sub-junction current generated from thermal effects in the baseline from the QD response. Both the 10 layer and 20 layer QD devices (Fig. 42 right) show approximately the same current contribution per QD layer.

Performance of the QD DJSCs under AM0 1-sun illumination has been measured to equal the efficiency of a baseline DJSC, see Fig. 43 which plots the devices with best efficiency and J_{sc} from each structure. Even though the QD DJSCs do not have higher efficiency than the best baseline DJSC, the QD DJSCs do maintain a higher J_{sc}, which can then be used for bandgap engineering in the full TJSC. Modeling effort for the duel and triple junction cells are discussed in Task 11.

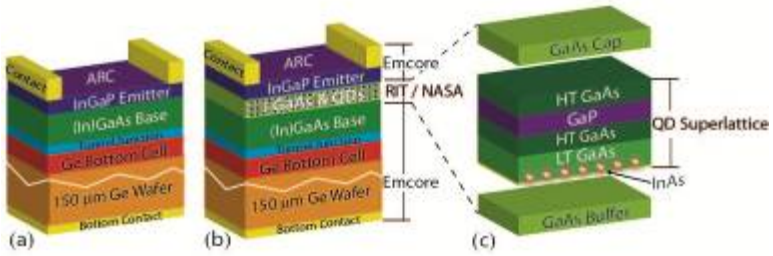

Fig. 41. Device structures of (a) a baseline double junction solar cell, (b) QD double junction solar cell, and (c) one repeat period of the QD superlattice.

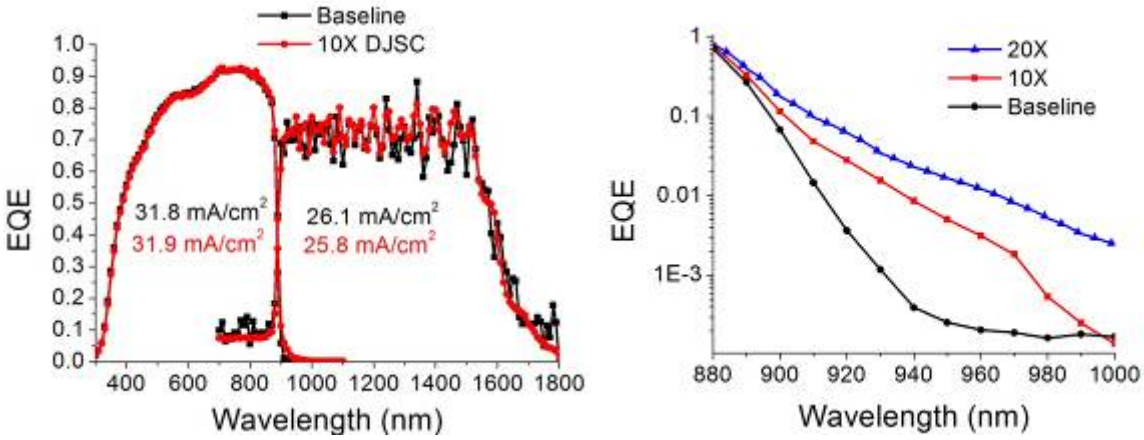

Fig. 42. (left) External quantum efficiency of GaAs/Ge double junction solar cell shows a sub-band gap current gain when 10 layers of QDs are incorporated in the i-region of the GaAs junction. (right) Detailed sub-bandgap response for both a 10 layer and 20 layer device.

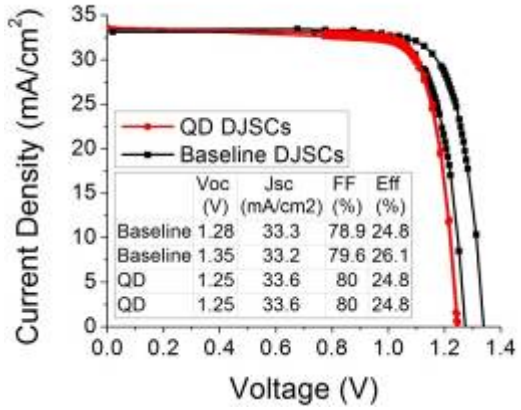

	Voc (V)	Jsc (mA/cm2)	FF (%)	Eff (%)
Baseline	1.28	33.3	78.9	24.8
Baseline	1.35	33.2	79.6	26.1
QD	1.25	33.6	80	24.8
QD	1.25	33.6	80	24.8

Fig. 43. Current-voltage curves and characteristics of double junction solar cells with and without 10 layers of QDs in the GaAs junction.

IX. **Task 9**: Strain-balanced approach will be applied to InGaAs QW growth. The QWs will be again inserted in i-region of GaAs pin cell. Temperature coefficients and spectral response of QW enhanced solar cells will be measured and correlated to both the numerical models and device design. Development of the QW cell will allow for comparison of both the QD vs. the QW approach.

Multi-quantum well (MQW) active regions in GaAs or InGaAs solar cells will utilize strained InGaAs QWs to extend the spectral response below that of the bulk cell material. In order to accommodate strain pseudomorphically, i.e., without dislocations, the MQW structural parameters (individual well width and strain, total number of wells) must be kept within limits based on strain energy balance. To this end, we have used our previously developed strain-compensation methods applied to a MQW region in which a tensile-strained barrier layer (InGaP) is placed between the compressively

strained InGaAs QW's. Fig. 44 shows a schematic of the proposed middle cell device with QW region highlighted.

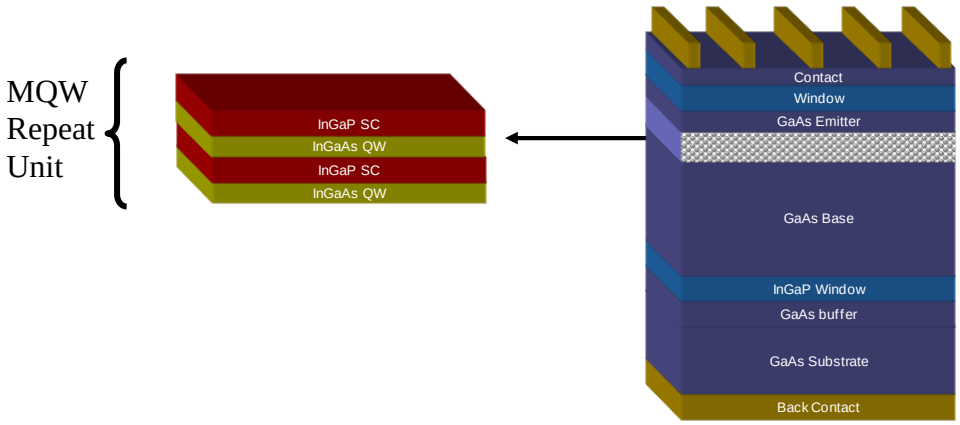

Fig. 44. Schematic solar cell structure incorporating InGaAs/InGaP strain compensated QWs.

Based on previous results and simulations, an optimized InGaAs-GaAsP-GaAs quantum well solar cell was grown at NASA Glenn. The thickness and composition of the QW and strain balance layer were adjusted to minimize residual stress. This result was confirmed through high resolution XRD (Fig. 45a). As can be seen, clear superlattice peaks are observed, with a net tensile superlattice strain of 216 ppm.

The cell was fabricated at RIT and results are shown below in Fig. 45b and c. The one sun light JV curve was compared to a baseline cell without QWs. There was a clear enhancement in J_{sc} compared to the baseline cell, but the loss in V_{oc} is more significant than seen previously in QD based devices. This is believed to be due to increase in dark current due to interface recombination in the i-region. Further growth optimization (temperature, gas flow switching) is necessary to achieve higher quality QW interfaces. However, the spectral response (Fig. 45c) does show a strong response due to absorption in the QW region (870-1000 nm). It is believed that V_{oc} can be improved with growth optimization and by further reduction of the tensile strain, perhaps allowing a slight compressive strain. The J_{sc} can be improved by increasing the QW stack beyond 10 layers.

Several aspects deserve ongoing effort beyond this project. First, is an increase in the number of QW periods. The strain balancing will become more important as the total number of layers increases – but the absolute increase in current will also increase and the additional current increase assumption needs to be verified. Additionally, band structure engineering of the QW/barrier combination has the potential to improve the gain in current per QW layer. Changing the barrier heights through different compositions can significantly enhance the current collection. Thirdly, improvement of the 1-sun AM1.5 response is required. Efforts to address this are currently underway through separate funding source.

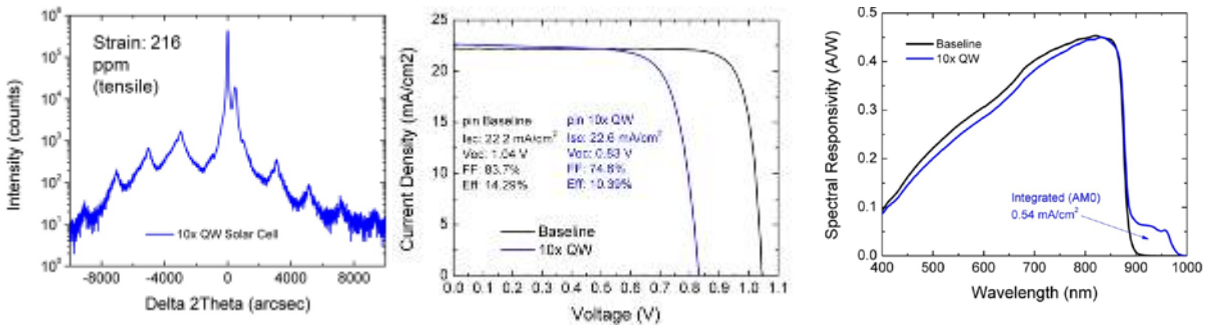

Fig. 45. X-ray (left), one sun AM1.5 JV curves (center) and spectral response (right) for QW solar cells fabricated through this project.

X. Task 10: Investigation of new cell designs based on doping of QDs. NanoTCAD modeling of the effect of InAs QD placed in flatband region of the cell and also placed near back surface field (tunnel junction). Growth, fabrication and characterization of QD enhanced cells with QDs placed in base and back field regions of GaAs pin solar cell.

A series of QD enhanced solar cells have been grown using Si delta doping. The delta-doping was incorporated for three 10X QD solar cells with Si doping over a 2nm layer of 0.4, 0.8 and 4.0 sccm equivalent silane flow. This corresponds to a delta doping of 1×10^{10} cm^{-2}, 2×10^{10} cm^{-2} and 1×10^{11} cm^{-2} , respectively. These cells were processed and investigated using one sun AM1.5g light IV, spectral response and electroluminescence to determine if doping improves the probability for intermediate band transitions into the conduction band (inter-subband absorption). Fig. 46 shows a comparison between all three wafers. V_{oc} and I_{sc} show uniform results among all three conditions. The higher doping condition has a slightly higher V_{oc} with lower I_{sc}. The largest increase in I_{sc} was observed for the 0.8 sccm equivalent silane flow.

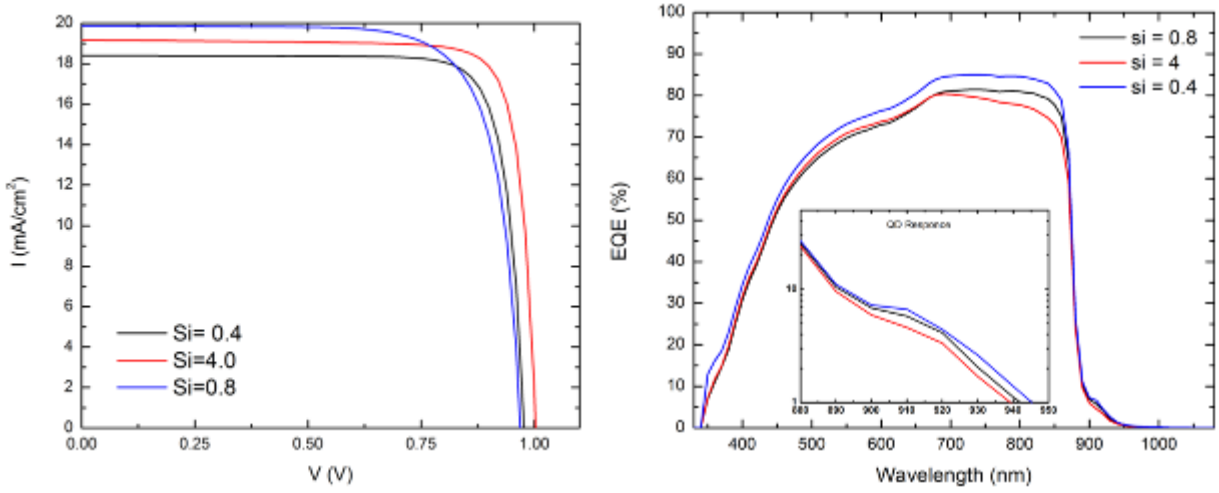

Fig. 46. a) one sun AM1.5g JV and b) quantum efficiency results from QD delta doping study.

Spectral response results show there could be material degradation within the base in the highest doping condition. QD response shows the delta doping has the best QD response in the lowest two doping conditions and the highest doping condition shows clear degradation in QD response. This study is being continued under the DoE Next Generation II program with UCLA.

XI. Task 11: Numerical modeling of full triple junction QD enhanced solar cell. Optimized design will be grown and fabricated. NanoTCAD modeling of full triple junction QW enhanced solar cell. Optimized design will be grown and fabricated. Measurements of both types of cells under concentration. Thermal and spectral characterization as before. Experimental results will be used as "feedback" for numerical models. Iteration until fully optimized QD/QW enhanced concentrator triple junction cell is achieved. Demonstrate >40% efficiency under concentration.

Modeling

Simulations for a baseline and 10-layer QD InGaP/GaAs/Ge triple junction (TJ) solar cell were performed in Crosslight and are depicted in Fig. 47. A measured current-voltage scan for a similar baseline device, which agrees well with simulation results, is included to demonstrate the suitability of the model. The total photocurrent generated from this tandem device is limited to the minimum photocurrent generated in a particular sub-cell to ensure current matching through the junctions. In this particular design, the middle GaAs sub-cell is current limiting as verified by the simulated current-voltage characteristics which show the full device J_{sc} is pinned at the level set by the GaAs current. As mentioned, one proposed route to increase the efficiency of the TJ solar cell is to increase the current generated in the limiting middle GaAs solar cell with the inclusion of QDs. Use of this geometry effectively lowers the bandgap of the middle cell so that more light can be harvested, resulting in an increase in the photocurrent. As a consequence, less infared light reaches the bottom junction and results in a decrease in the Ge sub-cell response. Evidence of this mechanism is supported by the simulations of the baseline and QD-enhanced TJ solar cell. In this device, 10 layers of QDs were embedded in intrinsic region of the middle cell. The total device J_{sc} increased from 16.47 to 16.69 mA/cm^2, resulting from a 0.22 mA/cm^2 increase in the GaAs sub-cell and 0.24 mA/cm^2 decrease from the Ge sub-cell. This result is further supported upon inspection of the individual junction quantum efficiencies where an increase in the sub-bandgap response of the GaAs sub-cell around 880-1100 nm commensurate with a decrease in the Ge sub-cell response for the same spectral region is observed. These simulations demonstrate the utility of incorporating quantum confined nanostructures in TJ solar cells and will serve as a design tool towards optimizing these structures.

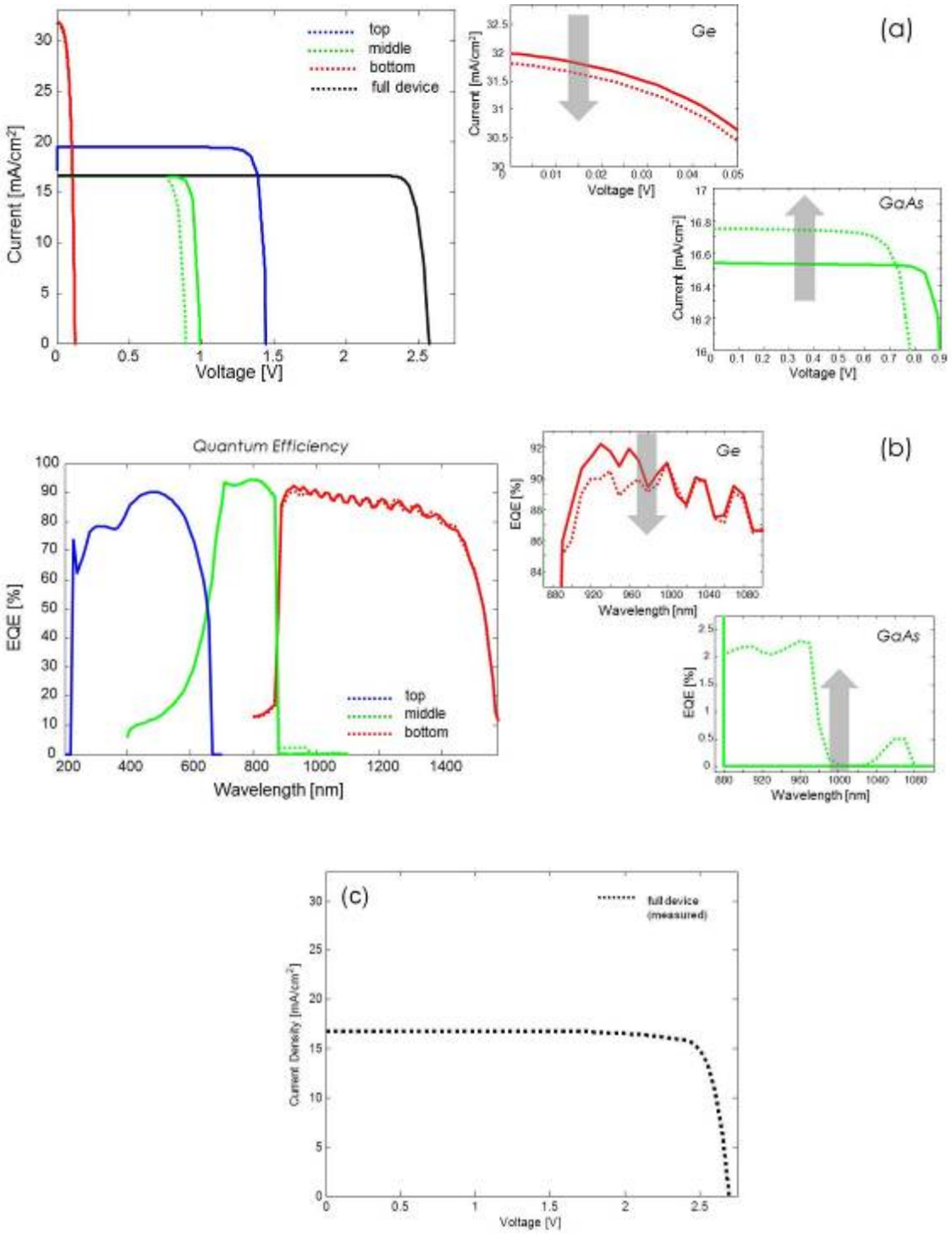

Fig. 47. (a) Current-voltage characteristics and (b) external quantum efficiency spectra for a InGaP/GaAs/Ge triple junction solar cells. The colored lines represent individual sub-cell responses: Ge (red), GaAs (green) and InGaP (blue). Dotted lines correspond to devices which include 10-layers of uncoupled QDs located in the intrinsic region of the middle GaAs sub-cell. The results for the GaAs and Ge sub-cells have been magnified to highlight the increase in the middle QD-enhanced GaAs cell (and corresponding decrease in the bottom Ge cell) photoresponse. (c) Measured current-voltage scan of baseline triple junction solar cell.

One-Sun Measurements of Triple Junction Solar Cells

Triple junction solar cells with and without quantum dots in the middle junction have been fabricated and characterized. The results for one-sun AM0 measurements, done with a two-zone close spectral match TS Space Systems simulator, are shown below. Fig. 48 compares the performance of 4 cm^2 baseline and 5X QD samples located at the same location on their respective wafer, in this case the voltage loss in the QD sample was compensated for by an increase in J_{sc} and FF. There are three positions on the wafer that showed the 5X QD outperforming the baseline. However, on average the baseline outperformed the 5X QD with values of 28.4% and 28.3% respectively. The slight decrease in average efficiency is due to an average voltage decrease in the 5X QD samples of 30 mV. However, with increasing number of QD layers, the increased J_{sc} can offset the 30mV loss in V_{oc}, leading to a greater efficiency improvement, as shown in Task 2 above.

Fig. 49 illustrates that the conversion efficiency in the junctions with and above the QD layers are unaffected. The plotted EQE also shows the increase in sub-band gap absorption and conversion in the middle junction due to the QD layers. The added current per QD layer, calculated by fitting the integrated current density of the EQE with the AM0 spectrum starting at 880 nm, is 0.024 mA/cm^2/QD layer.

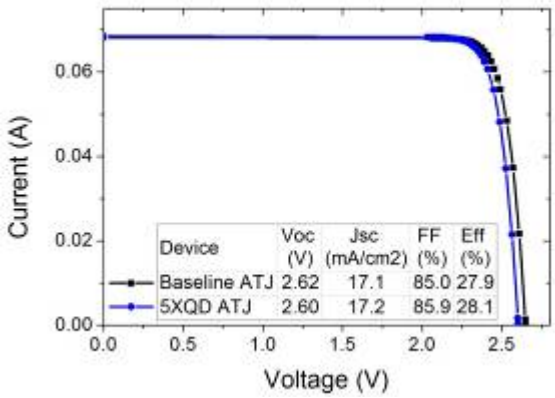

Fig. 48.. One-sun AM0 current-voltage plot and diode characteristics for a baseline and 5X QD triple junction solar cell.

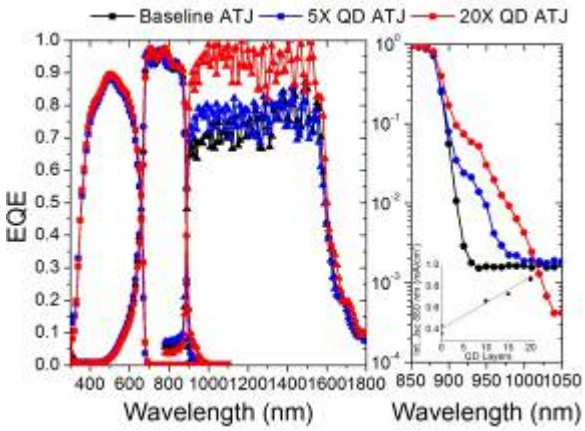

Fig. 49. External quantum efficiency measurements of triple junction solar cells with increasing number of QD layers. The sub-bandgap region, plotted on the right, shows the increase in sub-bandgap absorption and conversion due to increasing the number of QD layers.

A summary of the samples for official measurements performed at National Renewable Energy Laboratories PV Cell Performance Laboratory is listed in Table 6. The AM0 measurements were performed at RIT using the TS Space system solar simulator.

Table 6. Summary of one-sun AM0 IV characteristics

Sample	Description	AM0					
		Area cm^2	Isc mA	Jsc mA/cm^2	Voc V	FF %	Efficiency %
J7-7	Baseline ATJ	4.0	68.63	17.16	2.62	85.4	28.1
J7-10	Baseline ATJ	4.0	68.37	17.09	2.65	86.6	28.7
J17-7	5X QD ATJ	4.0	68.52	17.13	2.61	86.7	28.3
J17-4	5X QD ATJ	4.0	68.28	17.07	2.62	86.7	28.4
164581-W23-3	20X QD ATJ	4.0	67.90	16.97	2.53	86.2	27.1

Temperature Dependent Measurements of Triple Junction Solar Cells

Temperature Coefficients

Temperature coefficients for performance parameters of triple junction solar cells with and without 5 layers of quantum dots are extracted from 1-sun AM0 current-voltage measurements and external quantum efficiency measurements. Fig. 50 shows the baseline and QD triple junction solar cell structures used for this study.

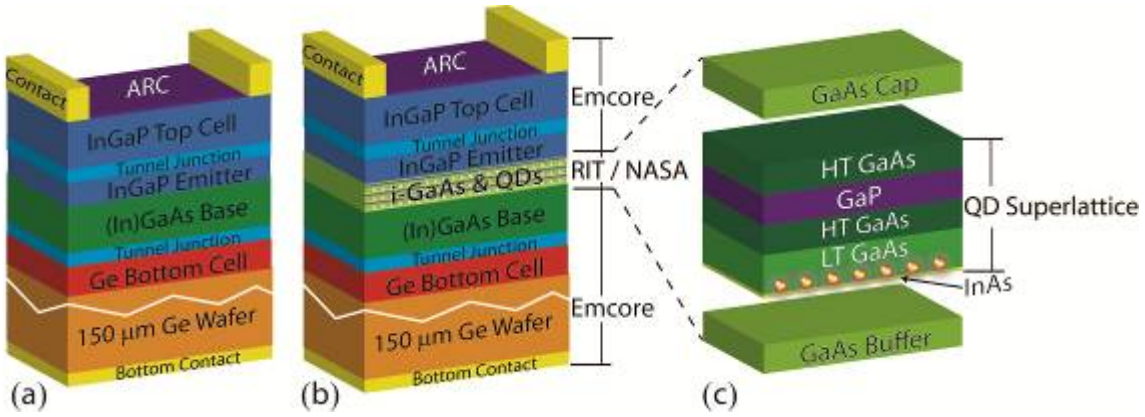

Fig. 50. Device structures of (a) a baseline triple junction solar cell, (b) QD triple junction solar cell, and (c) one repeat period of the QD superlattice.

The results are tabulated in Table 7 and the temperature dependent data is shown in Figs. 51 and 52. The combination of a lower $\Delta V_{oc}/^{o}C$ degradation and greater $\Delta J_{sc}/^{o}C$ increase leads to a lesser degradation in the maximum power output, P_{mp}, at higher temperatures. The improved temperature stability of QD triple junction solar cells may make them a more ideal device for high temperature environments, such as concentrator systems.

Table 7. Temperature coefficients calculated from AM0 1-sun measurements and external quantum efficiency measurements.

Device	**InGaP Integrated J_{sc} (ΔmA/cm^2)/°C**	**GaAs Integrated J_{sc} (ΔµA/cm^2)/°C**	**AM0 J_{sc} (ΔµA/cm^2)/°C**	**AM0 V_{oc} ΔmV/ ^{o}C**	**AM0 P_{mp} ΔmW/ ^{o}C**
Baseline	9.6	9.1	7.48	-6.4	-0.425
5X QD	9.7	8.3	9.53	-6.1	-0.385

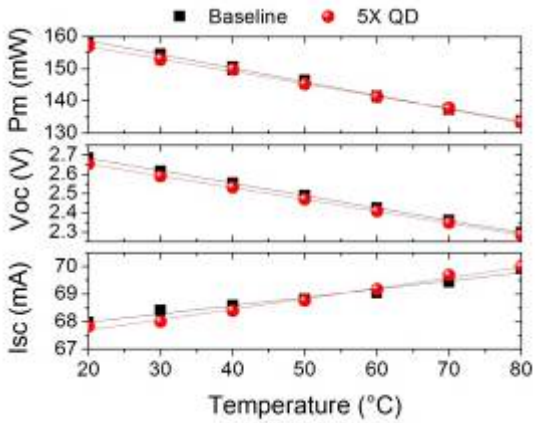

Fig. 51. Temperature dependent measurements under AM0 illumination are used to extract temperature coefficients for triple junction solar cells with and without 5 layers of QDs.

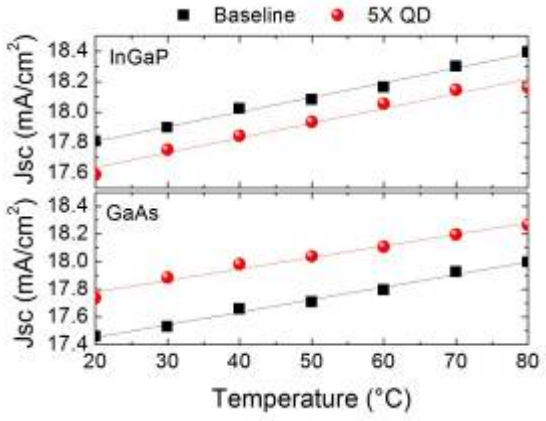

Fig. 52. Temperature dependent external quantum efficiency measurements are used to extract temperature coefficients for short circuit current of InGaP and GaAs sub-junctions in 5X QD and baseline triple junction solar cells.

Thermal Activation Energy

Determination of the effective thermal energy required for carriers to escape from quantum confined states was performed on a 5X QD triple junction solar cell by measuring the spectral luminescence with respect to temperature. This technique has been used on several QD material systems [9]. Increasing temperature allows more carrier escape via thermal excitation. Each peak in the spectral luminescence, seen in the inset of Fig. 53, corresponds to a specific quantum confined state. Luminescence from each peak is determined by fitting the curve then integrating the area for each peak. Thermal activation energy, E_a, is computed by fitting Equation 1 where c is the

exciton concentration and α is a fitting parameter that describes the effective scattering time from the high energy tail of the excition distribution in the quantum confined state into the barrier states, k_B is Boltzmann's constant and T is temperature.

$$PL(T) = \frac{c}{1+\alpha e^{-E_a/k_B T}} \quad (1)$$

The activation energy for the 930 nm peak is 167 meV and for the 960 nm peak 175 meV. It is expected that longer wavelength PL peaks have a greater thermal activation energy since their energy is less, meaning a greater amount of energy is required to reach the conduction band from the quantum confined state. The extracted activation energies were consistent with previous results for carrier escape from InAs QDs.

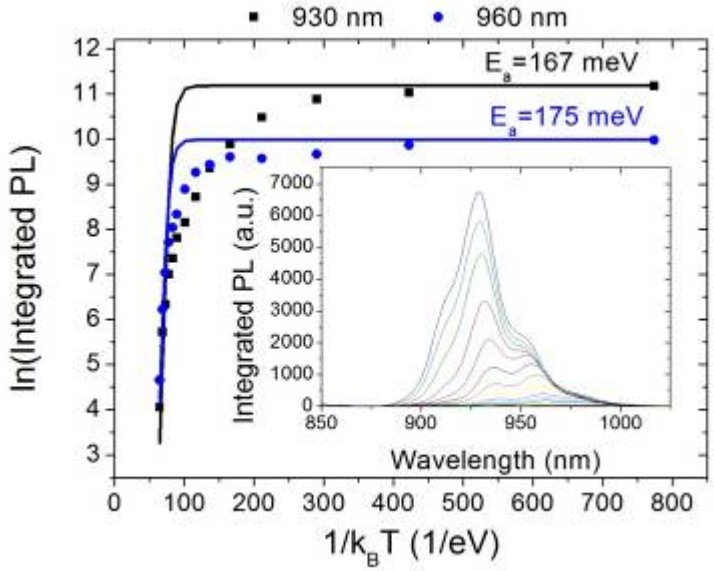

Fig. 53. Integrated photoluminescence signal from quantum states emitting at 930 nm and 960 nm (at 15K) plotted versus thermal energy. Fitting the plot yields a thermal activation energy of 167 meV for the 930 nm peak and 175 meV for the 960 nm peak.

Triple Junction Solar Cells Measured Under Concentrated Light

A large area pulse solar simulator (LAPSS) was used to measure a triple junction solar cell with and without 10 layers of QDs in the i-region of the GaAs junction. The results, shown in Fig. 54, for these measurements show the I_{sc} increase of the QD sample is slightly greater than that of the baseline device. Open circuit voltage of the baseline and QD samples are also close in terms of absolute values. These results show that QD solar cells can provide greater efficiency under concentration than baseline devices, as long as the quality of the QD solar cell is comparable to the baseline. However, TJSC devices were not fully optimized for concentration conditions, so efficiency began to degrade at a low (100X) concentration level.

Although we have not achieved 40% conversion efficiency under concentration, we would expect, based on the one sun efficiency of the QD TJSC, that at concentrations of 500 suns, multiple-layer QD TJSCs could realistically achieve over 40% conversion efficiency.

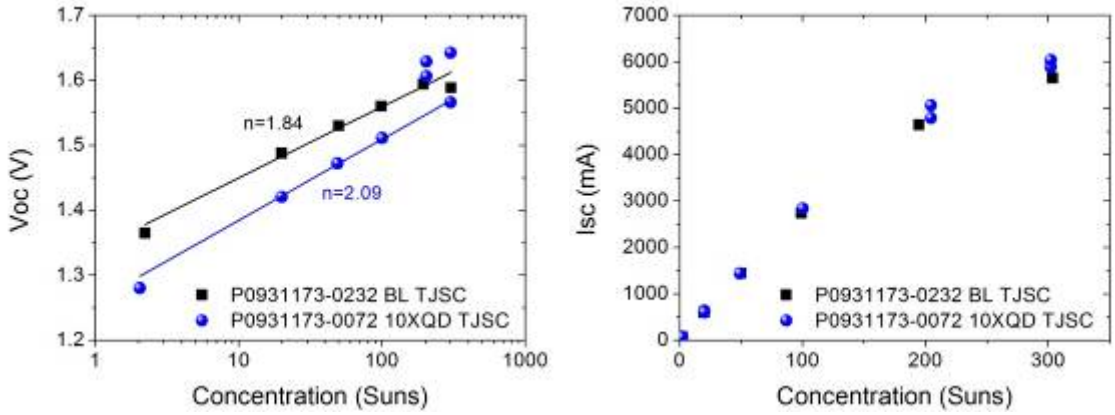

Fig. 54. Large area pulse simulator measurements of triple junction solar cells with and without 10 layers of QDs in the GaAs middle junction.

XII. Task 12: Delivery of 5 triple junction solar cells to NREL for independent testing and verification. Deliver 5 cells to III-V cell manufactures (Emcore and Spectrolab) and CPV system manufactures for demonstration of our enhanced triple junction cells using a commercial concentrator system. Working with the III-V cell manufactures, we will also assess the predicted scale-up costs specific to this particular cell development effort.

Five (5) TJSC were delivered to NREL for testing (see Task 11). These included 2 baseline devices without QDs, 2 QD enhanced TJSC with a 5 period QD superlattice and 1 QD enhanced TJSC with a 20 period QD superlattice. A summary of the one sun AM1.5 results are shown below. Copies of the individual IV curves are also shown in Fig. 55-57.

Table 8. Summary of one-sun AM1.5G IV characteristics performed at NREL.

		NREL one sun AM1.5					
		Area cm^2	Isc mA	Jsc mA/cm^2	Voc V	FF %	Efficiency %
J7-7	Baseline ATJ	3.976	46.932	11.795	2.5914	75.6	23.12
J7-10	Baseline ATJ	3.976	54.857	13.781	2.6157	80.9	29.17
J17-7	5X QD ATJ	3.976	55.216	13.888	2.5790	81.4	29.16
J17-4	5X QD ATJ	3.976	54.726	13.751	2.5891	81.3	28.95
164581-W23-3	20X QD ATJ	3.976	56.446	14.197	2.5026	80.2	28.49

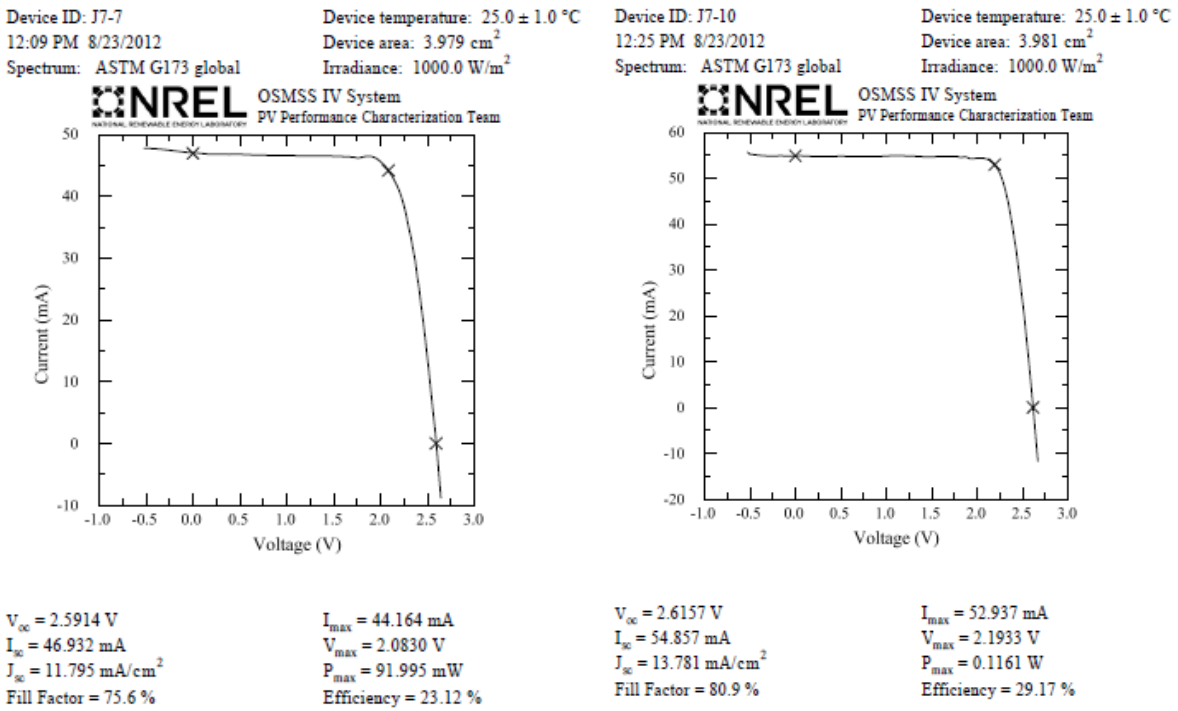

Fig. 55. Certified NREL one sun AM1.5 JV curves for the baseline triple junction devices without QDs.

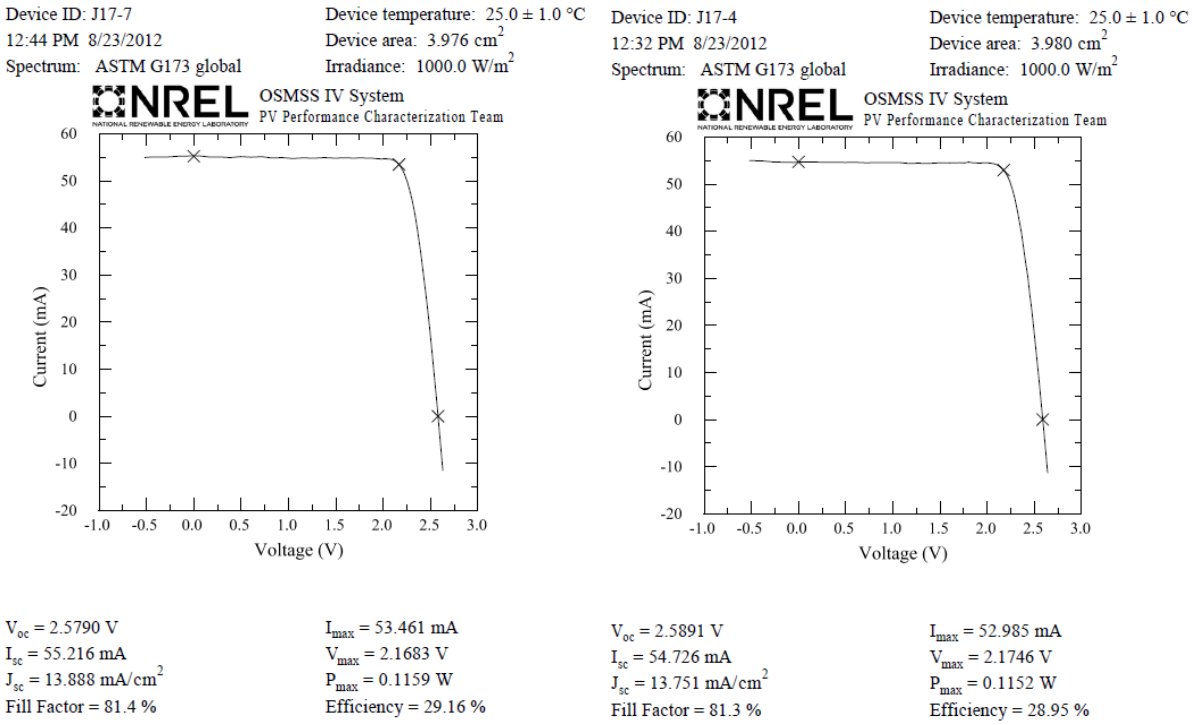

Fig. 56. Certified NREL one sun AM1.5 JV curves for the 5 period QD enhanced triple junction devices.

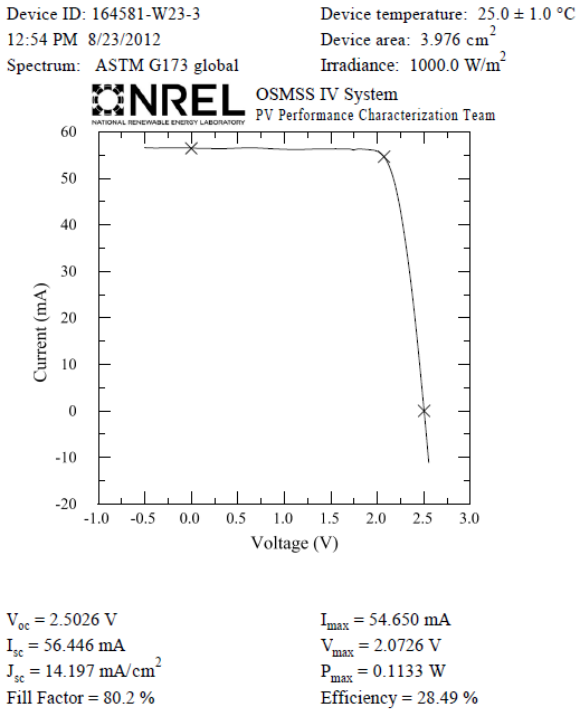

Fig. 57. Certified NREL one sun AM1.5 JV curves for the 20 period QD enhanced triple junction devices.

As can be seen in Table 8, the baseline and 5 period QD solar cells have almost identical efficiency. Although both QD solar cells have gains in current, as expected due to bandgap engineering in the middle junction, the loss in V_{oc} has mitigated the gains in J_{sc}, resulting in similar efficiencies. Note that the baseline cell J7-7 was likely damaged in shipping, as this cell was tested at RIT before shipping and performed at the same levels at J7-17. The main advantages of QD for the TJSC can still be seen, mainly the systematic increase in J_{sc} with addition of QD. Similar results were obtained at RIT under an AM0 spectrum as seen in Task 11.

Fig. 58 summarizes the quantum efficiency data received from NREL. The full QE for each sub-junction is shown in the left plot. A detailed plot of the sub-junction response of the middle junctions can be seen to the right. Middle cell response for all cells was similar except for the added QD response seen at wavelengths beyond 870nm. Addition of QD to the middle cell has extended the middle cell response, in the case of the 20 period device 1% EQE was still measured at 1000nm. Variation in the top cell response were see in one of the 5 period devices indicative of degradation in the top cell, while the second 5 period QD device and the 20 period device show similar top cell performance compared to the baseline.

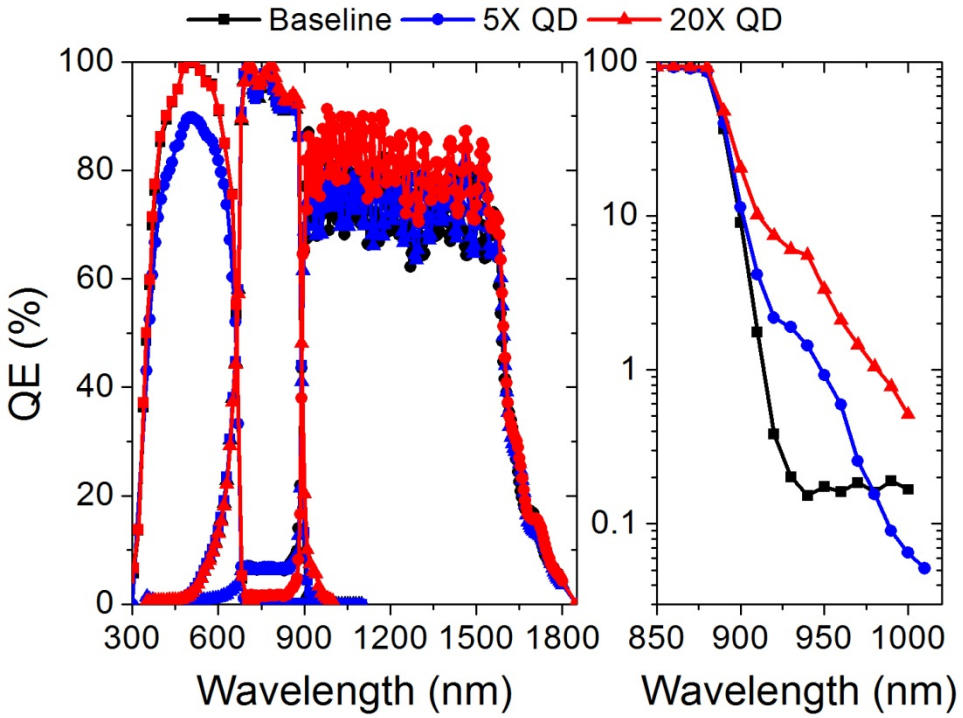

Fig. 58. Comparison of baseline, 5X, and 20X QD ATJ solar cells with InAs strained balanced QDs in the GaAs junction.

Values for the integrated short circuit current density of each junction are tabulated in Table 9. Three cells have the top two junctions current matched to less than 1% (a baseline, a 5X, and a 20X). The QD devices show a consistent increase in middle cell current compared to the baseline. However, the design of the cells could be further optimized by increasing the InGaP top cell response in order to force the middle cell to

be current limiting. In order to extract the QD contributed current, the QE was integrated at and greater than 880 nm. The results are shown in Figure 59. A liner fit give the QD contribution as 0.0142 mA/cm^2 per QD layer for the AM1.5G173-03 solar spectrum.

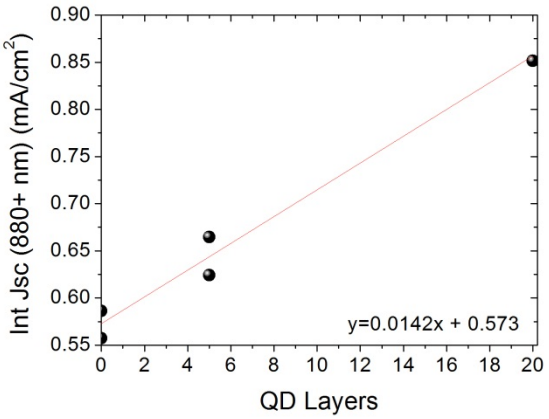

Fig. 59. Fitting the sub-band gap current generation shows each layer of QDs contributes 0.0142 mA/cm^2 per QD layer.

Table 9. Integrating the EQE measurements with the AM1.5G spectrum yields the current generation of each sub-junction. Bold values indicate the limiting current of the solar cell. *The Ge junction of J7-7 is presumed inaccurate due to shunting, which increases the complexity of attaining accurate QE data.

AM1.5G		Int J_{sc} (mA/cm^2)		
Sample	Description	InGaP	GaAs	Ge
164581	20X	**16.30**	16.36	19.69
J17-4	5X	16.14	**16.08**	19.19
J17-7	5X	**14.43**	15.97	18.83
J7-10	BL	16.24	**15.86**	18.44
J7-7	BL	16.16	**16.05**	9.80*

Overall, the results above show that the TJSC can be effectively engineered by addition of QDs into the middle GaAs sub-junction. However, in order to realize effective gains in efficiency, both QD absorption must be increased as well as mitigation of open circuit voltage loss. The effect of QD absorption and V_{oc} loss has been simulated in previous tasks.

The current set of TJSC devices were not optimized or fabricated on concentrator cells. Shown below in Table 10, a conservative estimate is given for QD TJSC operation at 1000 suns. This is based on linear increase in J_{sc}, logarithmic increase in V_{oc} and no change in FF. Again, the baseline and QD cells show almost identical efficiency. However, as seen in Task 11, Fig. 54, some degree of voltage recovery in the QD devices can be obtained at higher concentration. This is a similar effect as seen for many of the high efficiency Inverted Metamorphic concentrator cells and is likely due to high injection filling of defect states, thus increasing minority carrier lifetime.

Therefore, the QD devices have strong potential for net gains in efficiency at high concentration. Demonstration of this would require further optimization of the devices for concentration. We are currently investigating this effect through ongoing collaboration with Emcore. In addition, as a result of this funding, Emcore is investigating potential use of QDs in its triple junction devices.

Table 10. Summary of estimated 1000-sun AM1.5D IV characteristics

		Estimated 1000 sun AM1.5D performance		
		Jsc A/cm^2	Voc V	Efficiency %
J7-7	Baseline ATJ	10.6	3.07	27.4%
J7-10	Baseline ATJ	12.4	3.10	34.5%
J17-7	5X QD ATJ	12.5	3.06	34.5%
J17-4	5X QD ATJ	12.4	3.07	34.3%
164581-W23-3	20X QD ATJ	12.8	3.00	33.9%

Patents:

Invention disclosure filed with RIT legal affairs office on 11/24/2009. Invention title "Weighted Strain Balancing Procedure for Epitaxial Quantum Dot Growth".

Students Supported:

Chris Bailey, Ph.D Microsystems Engineering, 2012 RIT. Thesis title: *Optical and Mechanical Characterization of InAs Quantum Dot Array Embedded Devices.* Status: NRC Postdoctoral Fellow, Naval Research Laboratory.

Steve Polly, Ph.D Microsystems Engineering, RIT. Thesis title: *Characterization of Quantum Dot Photovoltaics*. Status: graduation anticipated in May 2014.

Yushuai Dai, MS Materials Science 2012, RIT. Thesis title: *Resonant Spectroscopy of quantum dot solar cells*. Status: Microsystems PhD student at RIT.

Chelsea Mackos, MS Materials Science, RIT 2011. Thesis Title: *Optimization of Concentrator GaAs Photovoltaic Devices with InAs Quantum Dots through Substrate*

Misorientation and Electroplating. Status: Senior Processing Engineer at Emcore Photovoltaics, Inc.

Joanne Oakvath, MS Electrical Engineering, RIT 2010. Thesis Title: *The Effects of GaAs Substrate Miscut on InAs Quantum Dot Optoelectronic Properties: Examined by Photoreflectance (PR) and Deep Level Transient Spectroscopy (DLTS).* Status: Senior Test Engineer at Fairchild Semiconductors.

Michael Harris, MS Electrical Engineering, RIT 2010. Thesis title: *Design and testing of high concentration quantum dot solar cells.* Status: Imaging Science PhD student, RIT.

Ryan Aguinaldo, MS Materials Science, RIT, 2009. Thesis Title: Modeling Solutions and Simulations for Advanced III-V Photovoltaics Based on Nanostructures. Status: Electrical Engineering PhD student at University of California San Diego.

Publications/Presentations/Travel:

Papers Published

S. M. Hubbard, C. Mackos, A. Podell, S. Polly, C. Bailey, and D. V. Forbes, "Effect of Vicinal Substrates on the Growth and Device Performance of Quantum Dot Solar Cells," Solar Energy Materials and Solar Cells, accepted and in-press, 2012.

C. G. Bailey, D. V. Forbes, S. J. Polly, Z. S. Bittner, Y. Dai, C. Mackos, R. P. Raffaelle, and S. M. Hubbard, "Open-Circuit Voltage Improvement of InAs/GaAs Quantum-Dot Solar Cells Using Reduced InAs Coverage," Photovoltaics, IEEE Journal of, vol. 2, pp. 269-275, 2012.

C. G. Bailey, D. V. Forbes, R. P. Raffaelle, and S. M. Hubbard, "Near 1 V open circuit voltage InAs/GaAs quantum dot solar cells," Applied Physics Letters, vol. 98, pp. 163105-3, 2011.

S. Hubbard, R. Raffealle, S. Bailey, “Quantum Dot Solar Cells”, in *Nanotechnology for Photovoltaics*, Ed. Loucas Tsakalakos, CRC Press:Boca Raton, 279-322, 2010.

C. Bailey, S. M. Hubbard, D. Forbes, and R. Raffaelle, "Evaluation of strain balancing layer thickness for InAs / GaAs QD arrays using HRXRD and Photoluminescence," *Applied Physics Letters* **95**, 203110 (2009).

S. M. Hubbard, C. Bailey, S. Polly, C. Cress, J. Andersen, D. Forbes, and R. Raffaelle, "Nanostructured photovoltaics for space power," *Journal of Nanophotonics* **3**, 031880-031816 (2009).

A. I. Fedoseyev, M. Turowski, A. Raman, E. W. Taylor, S. Hubbard, S. Polly, Q. Shao, and A. A. Balandin, "Space radiation effects modeling and analysis of quantum dot

based photovoltaic cells," *Nanophotonics and Macrophotonics for Space Environments III* **7467**, 746705-746710 (2009).

A. I. Fedoseyev, M. Turowski, A. Raman, Q. Shao, and A. A. Balandin, "Simulation of quantum dot-based nanodevices for photovoltaic applications with multiscale models," *International Journal for Multiscale Computational Engineering* **7**, 1-7 (2009)

SPIE Newsroom Press Release, “Solar cell efficiency is improved using quantum dot based nanotechnology”. DOI: 10.1117/2.1201002.002553

Q. Shao, A. A. Balandin, A. I. Fedoseyev, and M. Turowski, "Computational design of the intermediate-band solar cells based on the quantum dot superlattices," *Nanoscale Photonic and Cell Technologies for Photovoltaics* **7047**, 70470B-70478 (2008).

Papers in Preparation

K. Driscoll and S. Hubbard, "Modeling the optical and electrical response of nanostructured III-V solar cells," in preparation for Applied Physics Letters.

Christopher G. Bailey, David V. Forbes, Seth M. Hubbard, Ryne P Raffaelle, “Optical and mechanical properties of strain compensated InAs/GaAs quantum dot superlattices with varying InAs coverage” in preparation for Journal of Crystal Growth.

Invited Papers at National / International Meetings

S. M. Hubbard, C. G. Bailey, A. Podell, C. Mackos, D. V. Forbes, " Voltage Improvement in InAs Quantum Dot Solar Cells," in *Physics and Simulation of Optoelectronic Devices XX*, SPIE Photonics West, San Francisco, California, USA, 2012.

***Best Student Paper Award*:** C. G. Bailey, D. V. Forbes, R. P. Raffaelle, and S. M. Hubbard, "Open Circuit Voltage Improvement in InAs/GaAs Quantum Dot Solar Cells Using Reduced InAs Coverage," *Photovoltaic Specialists Conference (PVSC), 2011 37th IEEE*, 2011.

Seth M. Hubbard, Chelsea R. Mackos, Christopher G. Bailey, Stephen Polly, David V. Forbes, “GaAs Substrate Misorientation and the Effect on InAs Quantum Dot Solar Cells”, 22nd SPRAT Conference, NASA Glenn Research Center, Cleveland, OH, September 20-22, 2011.

Seth M. Hubbard, Christopher Bailey, Chelsea Plourde, Zac Bittner, David Forbes, “Invited: Epitaxial growth of quantum dots for photovoltaic application”, XIX International materials Research congress, Cancun, Mexico, August 15-19, 2010.

S.M. Hubbard, C. Bailey, S. Polly, M. Harris, C. Cress, D. Forbes, R. Raffaelle, “Characterization of Quantum Dot Enhanced Solar Cells under Solar Concentration”, SPRAT XXI, Cleveland, OH, October 6 2009.

S. M. Hubbard, C. Bailey, C. D. Cress, S. Polly, J. Clark, D. V. Forbes, R. P. Raffaelle, S. G. Bailey, D. M. Wilt, “Short circuit current enhancement of GaAs solar cells using strain compensated InAs quantum dots”, *33rd IEEE Photovoltaic Specialists Conf.* 1, pp. 1-6 (2008).

Contributed Papers at National / International Meetings

S. J. Polly, Z. S. Bittner, C. G. Bailey, Y. Dai, D. V. Forbes, and S. M. Hubbard, "Low Temperature Analysis of Quantum Dot Solar Cells," in *Photovoltaic Specialists Conference (PVSC), 2012 38th IEEE*, 2012, pp. 1-6.

S. J. Polly, C. G. Bailey, Z. S. Bittner, Y. Dai, E. G. Fernandez, and S. M. Hubbard, "Spectroscopic analysis of InAs quantum dot solar cells," in *Physics and Simulation of Optoelectronic Devices XX*, San Francisco, California, USA, 2012, pp. 825615-6.

S. M. Hubbard, A. Podell, M. Bennett, M. Slocum, and D. Forbes, "Optimization of Growth and Device Performance for InAs Quantum Dot Solar Cells," in *Photovoltaic Specialists Conference (PVSC), 2012 38th IEEE*, 2012, pp. 1-6.

D. Forbes, C. G. Bailey, S. Polly, Z. Bittner, C. Kerestes, M. Slocum, and S. M. Hubbard, "Correlation Between Quantum Dot Morphology and Photovoltaic Performance," in *Photovoltaic Specialists Conference (PVSC), 2012 38th IEEE*, 2012, pp. 1-6.

K. Driscoll and S. Hubbard, "Modeling the optical and electrical response of nanostructured III-V solar cells," in *Photovoltaic Specialists Conference (PVSC), 2012 38th IEEE*, 2012, pp. 1-6.

Best Poster Nominee: Y. Dai, C. G. Bailey, C. Kerestes, D. V. Forbes, and S. M. Hubbard, "Investigation of Carrier Escape Mechanism in InAs/GaAs Quantum Dot Solar Cells," in *Photovoltaic Specialists Conference (PVSC), 2012 38th IEEE*, 2012, pp. 1-6.

S. J. Polly, Z. Bittner, M. Bennett, R. Raffaelle, and S. Hubbard, "Development of a Multi-Source Solar Simulator for Spatial Uniformity and Close Spectral Matching to AM0 and AM1.5," in *Photovoltaic Specialists Conference (PVSC), 2011 37th IEEE*, 2011, pp. 1-6.

C. Mackos, D. Forbes, C. G. Bailey, S. J. Polly, and S. Hubbard, "GaAs Substrate Misorientation and the Effect on InAs Quantum Dot Critical Thickness," in *Photovoltaic Specialists Conference (PVSC), 2011 37th IEEE*, 2011, pp. 1-6.

C. Kerestes, S. Polly, D. Forbes, C. Bailey, S. Hubbard, J. Spann, P. Patel, and P. Sharps, "Investigation of quantum dot enhanced triple junction solar cells," in *Photovoltaic Specialists Conference (PVSC), 2011 37th IEEE*, 2011, pp. 000127-000132.

C. G. Bailey, D. V. Forbes, R. P. Raffaelle, and S. M. Hubbard, "Investigation of spectral responsivity of InAs QD-embedded GaAs solar cells," in *Physics and Simulation of Optoelectronic Devices XIX*, San Francisco, California, USA, 2011, pp. 793313-7.

C. G. Bailey, D. V. Forbes, R. P. Raffaelle, S. M. Hubbard, “Efficiency improvement using InAs QDs in GaAs single junction solar cells,” International Materials Research Conference (IMRC), Cancun, Mexico, Aug 14-19th, 2011.

C. G. Bailey, C. Kerestes, C. R. Mackos, S. J. Polly, D. V. Forbes, S. M. Hubbard, “Effects of vicinal substrates and InAs growth parameters for InAs QD/GaAs Solar Cells,” International Materials Research Conference (IMRC), Cancun, Mexico, Aug 14-19th, 2011.

Stephen J. Polly, Zachary S. Bittner, Aymeric Maros, Mitch F. Bennett, David A. Scheiman, Ryne P. Raffaelle, and Seth M. Hubbard, “Development of a Multi-Source Solar Simulator for Spatial Uniformity and Close Spectral Matching to AM0 and AM1.5”, 22nd SPRAT Conference, NASA Glenn Research Center, Cleveland, OH, September 20-22, 2011.

C. G. Bailey, Y. Dai, D. V. Forbes, R. P. Raffaelle, S. M. Hubbard, “Investigation and Recent Improvements of InAs/GaAs QD Solar Cells,” 22nd SPRAT Conference, NASA Glenn Research Center, Cleveland, OH, September 20-22, 2011.

Christopher G. Bailey, David V. Forbes, Ryne P. Raffaelle, Seth M. Hubbard, “Open Circuit Voltage Restoration in InAs QD Embedded GaAs p-i-n Solar Cells”, *Materials Research Society Fall Meeting*, Boston, MA, Nov. 29-Dec 3, 2010.

S. J. Polly, M. L. Harris, Z. Bittner, C. R. Plourde, C. G. Bailey, D. V. Forbes, and S. M. Hubbard, "Effect of cell size on GaAs concentrators with InAs quantum dots," in *Photovoltaic Specialists Conference (PVSC), 2010 35th IEEE*, 2010, pp. 002057-002061.

S. M. Hubbard, C. Plourde, Z. Bittner, C. G. Bailey, M. Harris, T. Bald, M. Bennett, D. V. Forbes, and R. Raffaelle, "InAs quantum dot enhancement of GaAs solar cells," in *Photovoltaic Specialists Conference (PVSC), 2010 35th IEEE*, 2010, pp. 001217-001222.

D. V. Forbes, S. M. Hubbard, C. Bailey, S. Polly, J. Andersen, and R. Raffaelle, "III-V quantum dot enhanced photovoltaic devices," in *Next Generation (Nano) Photonic and*

Cell Technologies for Solar Energy Conversion, San Diego, California, USA, 2010, pp. 77720C-10.

D. V. Forbes, C. G. Bailey, S. Polly, C. Plourde, J. Okvath, S. M. Hubbard, and R. P. Raffaelle, "Substrate orientation effects on quantum dot enhanced GaAs solar cells," in *Photovoltaic Specialists Conference (PVSC), 2010 35th IEEE*, 2010, pp. 001804-001807.

A. I. Fedoseyev, M. Turowski, A. Raman, E. W. Taylor, S. Hubbard, S. Polly, and A. A. Balandin, "Investigation and modeling of space radiation effects in quantum dot solar cells," in *Photovoltaic Specialists Conference (PVSC), 2010 35th IEEE*, 2010, pp. 002533-002536.

C. G. Bailey, S. J. Polly, J. Okvath, D. V. Forbes, C. D. Cress, S. M. Hubbard, and R. P. Raffaelle, "Temperature dependent photoluminescence spectroscopy of InAs/GaAs solar cells," in *Photovoltaic Specialists Conference (PVSC), 2010 35th IEEE*, 2010, pp. 000364-000369.

Seth M. Hubbard, Christopher Bailey, Joanne Okvath, Tim Bald, David Forbes, Ryne P. Raffaelle, "Thermal and Spectral Characteristics of Quantum Dot Solar Cells", *Materials Research Society Fall Meeting*, Boston, MA, Nov. 30, 2009.

Stephen J. Polly, Christopher G. Bailey, Michael L. Harris, David V. Forbes, Ryne P. Raffaelle, Seth M. Hubbard, "Reduction of Power Loss Mechanisms in InAs/GaAs QD Concentrator Solar Cell Grid Design", *Materials Research Society Fall Meeting*, Boston, MA, Nov. 30, 2009.

Christopher G. Bailey, Stephen J. Polly, David V. Forbes, Seth M. Hubbard, Ryne P. Raffaelle, "Effect of Barrier Thickness on Interband Transition Energies InAs/GaAs QD Solar Cells", *Materials Research Society Fall Meeting*, Boston, MA, Nov. 30, 2009.

Seth M. Hubbard, Christopher Bailey, Stephen Polly, Ryan Aguinaldo, David Forbes, Ryne Raffaelle, "Characterization of Quantum Dot Enhanced Solar Cells for Concentrator PV", Proc. of 34th IEEE Photovoltaic Specialists Conference, vol.1, pp. 1-6 (2009).

Christopher G. Bailey, Ryan Aguinaldo, Cory D. Cress, Stephen J. Polly, David V. Forbes, Seth M. Hubbard, Ryne P. Raffaelle, "Effect of barrier thickness on InAs QD / GaAs solar cells", Proc. of 34th IEEE Photovoltaic Specialists Conference, vol. 1, pp. 1-6 (2009).

***Best Student Paper Award*:** Michael L Harris, Seth M Hubbard, Michael S Kassis, Stephen J Polly, Christopher G Bailey, Paul R Jarosz, "Electroplating as Economical Means to Lower Series Resistance in GaAs Concentrator Solar Cells", Proc. of 34th IEEE Photovoltaic Specialists Conference, vol. 1, pp. 1-6 (2009).

Cory D. Cress, Seth M. Hubbard, Christopher G. Bailey, Ryne P. Raffaelle, Scott R. Messenger, Robert J. Walters, David V. Forbes, “Analysis of Strain Compensated GaAs-based InAs QD Solar Cells”, Proc. of 34th IEEE Photovoltaic Specialists Conference, vol. 1, pp. 1-6 (2009).

David V Forbes, Chris G Bailey, Stephen Polly, Seth M Hubbard, Ryne P Raffaelle, William F Maurer, “The Effect of Te as a Surfactant on OMVPE of InAs Quantum Dots”, Proc. of 34th IEEE Photovoltaic Specialists Conference, vol. 1, pp. 1-6 (2009).

Jamie R. Gardner, Eric K. Albers, Chris G. Bailey, Seth M. Hubbard, Ryne P. Raffaelle, “Thermal and spectroscopic characterization of quantum dot-enhanced solar cells”, Proc. of 34th IEEE Photovoltaic Specialists Conference, vol. 1, pp. 1-6 (2009).

Q. Shao, A.A. Balandin, “Three-Dimensional Quantum Dot Supra-Crystals for Photovoltaic Energy Conversion”, *Materials Research Society Spring Meeting*, San Francisco, MA, April 13-17, 2009.

Christopher Bailey, Seth Hubbard, David Forbes, Ryne P. Raffaelle, “Experimental Analysis of Out-of-Plane Strain Neutrality in Multilayer Quantum Dot Embedded p/i/n Diodes”, *Materials Research Society Spring Meeting*, San Francisco, MA, April 13-17, 2009.

Seth M. Hubbard, Christopher Bailey, Stephen Polly, Eric Albers, Ryan Aguinaldo, Cory Cress, John Anderson, David Forbes, Ryne P. Raffaelle, “Behavior of Quantum Dot Enhanced Photovoltaics under Solar Concentration”, *Materials Research Society Fall Meeting*, Boston, MA, December 1-5, 2008.

Ryne Raffaelle, Christopher Bailey, Seth Hubbard, Stephen Polly, and David Forbes, “Quantum Dot Spectral Tuning of Multijunction III-V Solar Cells”, Materials Research Society Fall Meeting, Boston, MA, December 1-5, 2008.

References

[1] S. M. Hubbard, C. D. Cress, C. G. Bailey, R. P. Raffaelle, S. G. Bailey, and D. M. Wilt, "Effect of strain compensation on quantum dot enhanced GaAs solar cells," *Appl. Phys. Lett.*, vol. 92, p. 123512, 2008.

[2] S. M. Hubbard, R. Raffaelle, R. Robinson, C. Bailey, D. Wilt, D. Wolford, W. Maurer, and S. Bailey, "Growth and Characterization of InAs Quantum Dot Enhanced Photovoltaic Devices," in *Mater. Res. Soc. Symp.*, 2007, pp. DD13-11

[3] C. G. Bailey, S. M. Hubbard, D. V. Forbes, and R. P. Raffaelle, "Evaluation of strain balancing layer thickness for InAs/GaAs quantum dot arrays using high resolution x-ray diffraction and photoluminescence," *Applied Physics Letters,* vol. 95, pp. 203110-3, 2009.

[4] M. L. Harris, S. M. Hubbard, M. S. Kassis, S. J. Polly, C. G. Bailey, and P. R. Jarosz, "Electroplating as Economical Means to Lower Series Resistance in GaAs Concentrator Solar Cells," presented at the 34th IEEE Photovoltaic Specialists Conf., 2009.

[5] H. J. Hovel and J. M. Woodall, "The effect of depletion region recombination currents on the efficiencies of Si and GaAs solar cells," in *10th Photovoltaic Specialist Conference*, 1973, p. 25.

[6] S. Tomic, T. S. Jones, and N. M. Harrison, "Absorption characteristics of a quantum dot array induced intermediate band: Implications for solar cell design," *Applied Physics Letters*, vol. 93, p. 263105, 2008.

[7] J. Nelson, *The physics of solar cells*. London: Imperial College Press, 2003.

[8] Q. Shao, A. A. Balandin, A. I. Fedoseyev, and M. Turowski, "Intermediate-band solar cells based on quantum dot supracrystals," *Applied Physics Letters*, vol. 91, pp. 163503-3, 2007.

[9] S. Fafard, S. Raymond, G. Wang, R. Leon, D. Leonard, S. Charbonneau, J. L. Merz, P. M. Petroff, and J. E. Bowers, "Temperature effects on the radiative recombination in self-assembled quantum dots," *Surface Science*, vol. 361–362, pp. 778-782, 1996.